physchem

MDPI

Article

Green Synthesis of Gold Nanoparticles Using *Kalanchoe pinnata* Leaf Extract: One-Factor Screening and Multivariable Optimization of Surface Plasmon Resonance Responses

Saideep Mallepaka [1], Himabindu Kurra [2], Aditya Velidandi [2], Pradeep Kumar Gandam [3], Swati Dahariya [4] and Vikram Godishala [1,2,*]

[1] Department of Biotechnology, Bharatiya Engineering Science and Technology Innovation University, Gorantla Mandal 506001, India; 2023wpbte001@bestiu.edu.in
[2] Department of Biotechnology, Vaagdevi Degree and P.G. College, Warangal 506001, India; bindukurrabiotechnologyhod@vaagdevicolleges.com (H.K.); adityabiotechnology@vaagdevicolleges.com (A.V.)
[3] Department of Biotechnology, National Institute of Technology, Warangal 506004, India; biopradeep1@gmail.com
[4] Department of Biochemistry, School of Life Sciences, University of Hyderabad, Hyderabad 500019, India; swati@uohyd.ac.in
* Correspondence: dr.g.vikram@vaagdevicolleges.com

Abstract

This study presents a statistically optimized protocol for the green synthesis of gold nanoparticles (Au NPs) using aqueous *Kalanchoe pinnata* leaf extract (AKPLE). An integrated experimental strategy, transitioning from preliminary one-factor-at-a-time (OFAT) screening to a five-factor Box–Behnken Design, was employed to model and simultaneously optimize two critical optical responses derived from surface plasmon resonance: the peak position (λ_{max}) and its absorbance intensity. Highly predictive quadratic models ($R^2 > 0.97$) revealed that synthesis outcomes are governed by significant nonlinear curvature, with minimal interaction effects. Multi-response optimization via a desirability function identified a harmonized set of conditions ($HAuCl_4$: 0.44 mM, AKPLE: 3.50% v/v, temperature: 80.6 °C, pH: 7.2, time: 66.7 min) predicted to minimize λ_{max} at 540 nm while maximizing absorbance to 0.61. Synthesis under these optimized conditions successfully produced spherical, crystalline Au NPs, as confirmed by characterization (average TEM size: 26.3 ± 4.1 nm; zeta potential: –30.45 mV). This work demonstrates that a hybrid OFAT-RSM approach is superior for the precise, multivariate optimization of plant-mediated Au NP synthesis, providing a validated and scalable framework to balance nanoparticle size and plasmonic intensity—an outcome unattainable through conventional OFAT methods.

Keywords: Box–Behnken design; gold nanoparticles; green synthesis; *Kalanchoe pinnata*; statistical optimization; surface plasmon resonance

Check for updates

Academic Editor: Alexander V. Eletskii

Received: 27 February 2026
Revised: 17 March 2026
Accepted: 3 April 2026
Published: 7 April 2026

Copyright: © 2026 by the authors. Licensee MDPI, Basel, Switzerland. This article is an open access article distributed under the terms and conditions of the Creative Commons Attribution (CC BY) license.

1. Introduction

Gold nanoparticles (Au NPs) have attracted extensive scientific interest due to their unique optical, electronic, catalytic, and biological properties, which arise from their surface plasmon resonance (SPR) behavior [1]. These characteristics make Au NPs highly suitable for applications in sensing, drug delivery, imaging, and catalysis [2,3]. Traditionally, Au NPs are synthesized through physical and chemical methods, which often involve hazardous reducing agents, high energy consumption, and toxic byproducts, raising environmental and safety concerns [4,5]. In response, green synthesis approaches using plant

extracts have emerged as sustainable alternatives, leveraging natural phytochemicals as both reducing and stabilizing agents [6,7]. Among various botanical sources, *Kalanchoe pinnata* (commonly known as Bryophyllum) has shown considerable potential due to its rich composition of flavonoids, phenolic acids, and other bioactive compounds capable of facilitating nanoparticle formation [8–10]. However, the synthesis process is influenced by multiple interdependent factors, and achieving optimal NP properties requires systematic investigation and control of these variables [11–13].

While green synthesis offers a sustainable alternative, achieving precise control over NP properties remains a significant challenge. A survey of the literature reveals a heavy reliance on the one-factor-at-a-time (OFAT) methodology for initial optimization [11–19]. This approach, while useful for identifying preliminary ranges, is inherently limited as it fails to capture the synergistic or antagonistic interactions between critical synthesis parameters, such as precursor concentration, extract volume, pH, temperature, and reaction time. Consequently, OFAT-derived 'optima' are often suboptimal, leading to inconsistent results and hindering reproducibility. Although response surface methodology (RSM) has been employed to address this [19–23], its application is frequently restricted to a limited number of factors (often two to three) and is primarily focused on maximizing a single output, typically absorbance. This overlooks the practical need to balance multiple, often competing, nanoparticle characteristics—such as minimizing size while maximizing absorbance—which is essential for tailoring NPs for specific applications.

To address this gap, we present an integrated experimental strategy for the green synthesis of Au NPs using aqueous *K. pinnata* leaf extract (AKPLE). This study transitions from OFAT screening to a comprehensive five-factor, three-level Box–Behnken Design (BBD), enabling the modeling of complex nonlinear effects. Its distinctive contribution is the concurrent optimization of two critical and competing optical responses—SPR peak position (λ_{max}) and its absorbance intensity—via a desirability function approach. This work moves beyond conventional single-response optimization to deliver a statistically validated, harmonized protocol that balances nanoparticle size and plasmonic intensity. The resulting predictive models and characterized nanoparticles provide a robust and scalable framework for advancing reproducible, application-specific plant-mediated nanofabrication.

2. Materials and Methods

2.1. Materials

Chloroauric acid trihydrate ($HAuCl_4 \cdot 3H_2O$), hydrochloric acid, sodium hydroxide, and 0.22 µm polyvinylidene difluoride syringe filters were obtained from HiMedia Laboratories Pvt. Ltd. (Hyderabad, India). All experiments utilized deionized water, with a pH between 6.8 and 7.2. Where necessary, the pH of solutions was adjusted with 1 M sodium hydroxide or 1 M hydrochloric acid. Stock solutions were prepared and diluted as needed using deionized water. Prior to use, all glassware was washed with a nonionic detergent, thoroughly rinsed with deionized water, and dried in a hot air oven.

Fresh leaves of *K. pinnata* were gathered in June 2025 from a residential area in Ooty, Tamil Nadu, India. The leaves exhibited a bright light-green hue, signifying their early developmental stage and vigorous health. After collection, they were rinsed repeatedly with deionized water, cleansed with ethanol, and then allowed to air-dry in the shade under sterile conditions at room temperature. Once dried, the leaves were ground into a fine powder using a household mixer.

2.2. Extract Preparation

The AKPLE was prepared by suspending 6 g of the powdered leaves (no sieving or particle size characterization was performed) in 100 mL of deionized water. This mixture

was incubated for 2 days at 37 °C in an orbital shaker (250 rpm) incubator (REMI, Mumbai, India). Following incubation, the extract was filtered sequentially through Whatman no. 1 filter paper (Sigma-Aldrich Ltd., St. Louis, MO, USA) and a 0.22 µm polyvinylidene difluoride syringe filter. The resulting filtrate (AKPLE) exhibited a light green color and an intrinsic pH of approximately 6.5, which was stored at 4 °C for subsequent use [24].

2.3. Nanoparticle Synthesis

$HAuCl_4$ served as the gold precursor for nanoparticle synthesis. The reaction was initiated by combining the AKPLE with 1 mL of $HAuCl_4$ solution in 1.5 mL microcentrifuge tubes and incubating at room temperature for 30 min. The $HAuCl_4$ and extract were used as mentioned in Section 2.3.1. The formation of Au NPs was visually confirmed by a color change from colorless to purple and spectroscopically monitored using UV-Vis spectroscopy between 400 and 700 nm. Post-incubation, the Au NPs were isolated by centrifugation at 15,000 rpm (20,630× *g*; KUBOTA 3300, Table-top Micro Centrifuge; RA-2024; Osaka, Japan) for 5 min. The resulting pellets were washed with deionized water and re-centrifuged, a process repeated 3 times to remove residual reactants. Finally, the purified pellets were dried overnight at 70 °C in a hot air oven [24]. The dried material was then collected for characterization and subsequent experiments.

2.3.1. One-Factor-at-a-Time Method

To investigate the effect of key parameters on the synthesis of Au NPs, 5 factors were systematically examined: the concentration of the gold precursor, the concentration of the plant extract (AKPLE), the reaction temperature, the reaction pH, and the reaction time. In each set of experiments, all parameters except the 1 being tested were held constant. The optimal $HAuCl_4$ concentration was determined by testing a range from 0.25 to 2.00 mM, while keeping the extract concentration at 2% v/v, the reaction at room temperature, the pH at 6.5, and the time at 30 min. Subsequently, the influence of the AKPLE concentration was evaluated by using specific volumes (5, 10, 15, 20, 25, 30, 35, and 40 µL) of the stock extract to achieve final concentrations of 0.5% to 4.0% v/v in the reaction mixture. This experiment was conducted at room temperature, pH 6.5, for 30 min and employed the optimal $HAuCl_4$ concentration identified in the previous step. Next, the effect of reaction temperature was studied by performing the synthesis from room temperature up to 100 °C, using the previously optimized concentrations of $HAuCl_4$ and extract, with a constant reaction time of 30 min. The impact of pH was then assessed by adjusting the reaction medium to pH values of 3, 5, 7, 9, and 11. These reactions were run for 30 min at the optimal temperature and precursor concentrations determined earlier. Finally, the influence of reaction time was studied over a period of 0 to 120 min, under the optimized conditions for all other parameters (precursor concentration, extract concentration, reaction temperature, and reaction pH).

2.3.2. Statistical Optimization

RSM was applied to model and optimize the green synthesis conditions for Au NP formation using Design-Expert® software (version 11; Stat-Ease Inc., Minneapolis, MN, USA). RSM was selected because the formation of plasmonic NPs in plant-mediated systems is typically governed by multiple synthesis variables that act simultaneously and often in a nonlinear manner; therefore, optimization based on factorial curvature and predictive modeling is more appropriate than sequential OFAT adjustments. A BBD was adopted because it efficiently estimates second-order (quadratic) response surfaces with a relatively small number of experiments and avoids combinations where all factors are simultaneously at extreme settings, which can be impractical or can drive unstable NP growth and aggregation. The experimental matrix was generated in a randomized run

order to minimize systematic error arising from uncontrolled time-dependent effects such as reagent aging, ambient variation, or instrument drift. No blocking was used.

The BBD comprised 46 experimental runs, including 6 replicated center points. Center-point replication was included to provide an unbiased estimate of pure experimental error and to enable formal lack-of-fit testing during model diagnostics. Five synthesis factors were investigated as continuous numeric variables within ranges established from the OFAT optimization experiments reported in Section 2.3.1, ensuring that the selected windows were practically feasible and spanned the region where measurable response variation and curvature were expected. $HAuCl_4$ concentration (factor A) was varied from 0.25 to 0.75 mM; AKPLE concentration (factor B) from 2.00 to 3.50% (*v*/*v*); temperature (factor C) from 70 to 90 °C; pH (factor D) from 5 to 9; and reaction time (factor E) from 30 to 90 min. Each factor was studied at 3 coded levels (−1, 0, +1), where the coded center level (0) corresponded to 0.50 mM $HAuCl_4$, 2.75% (*v*/*v*) AKPLE, 80 °C, pH 7, and 60 min. These center settings were selected near the midpoints of the feasible operating space to support stable estimation of linear and quadratic effects across the design domain.

NP formation and optical characteristics were quantified using UV–Vis spectroscopy, employing 2 responses derived from the SPR band. For each experimental run, the reaction mixture was transferred to a 1 cm path-length cuvette and scanned from 400 to 800 nm using a UV–Vis spectrophotometer (Shimadzu, Kyoto, Japan). The primary response (R1) was the SPR peak position, recorded as the wavelength of maximum absorbance (λ_{max}, nm). This parameter is widely used as an optical indicator of changes in an NP population, including shifts commonly associated with changes in effective particle size, dispersion state, and interparticle coupling. The secondary response (R2) was the absorbance at λ_{max}, recorded as the peak intensity at the SPR maximum under consistent measurement conditions. This intensity response serves as a relative indicator of the extent and strength of NP formation, reflecting the development of the plasmonic band and the optical density contributed by the NP population.

For each response, experimental data were fitted independently to a second-order polynomial model incorporating linear, 2-factor interaction, and quadratic terms. The general quadratic model used is presented in Equation (1).

$$Y = \beta_0 + \sum \beta_i X_i + \sum \beta_{ij} X_i X_j + \sum \beta_{ii} X_i^2 \quad (1)$$

where (Y) denotes the response (λ_{max} or absorbance at λ_{max}), (X_i) denotes the coded factor values for A to E, and the regression coefficients represent the intercept, linear effects, interaction effects, and squared effects. The coded-factor form was retained for coefficient interpretation because coding standardizes the factor scales and allows direct comparison of coefficient magnitudes across variables. Model adequacy and term significance were assessed using analysis of variance (ANOVA), including evaluation of overall model significance and lack-of-fit relative to pure error obtained from the replicated center points. Residual diagnostics and predictive statistics were considered to ensure that the selected models were suitable for navigating the experimental region and supporting optimization.

Multi-response numerical optimization was subsequently implemented using the desirability function approach in Design-Expert. In this optimization, factor settings were constrained to remain within the experimentally studied bounds to avoid extrapolation. The goal for λ_{max} was defined as minimization (to favor a shorter-wavelength SPR maximum consistent with smaller and/or better-dispersed particles within the optical proxy framework), while the goal for absorbance at λ_{max} was defined as maximization (to favor a strong SPR intensity consistent with robust NP formation). The desirability framework converts each response into a scaled desirability value and identifies factor settings that maximize the overall desirability across the simultaneous objectives.

2.4. Nanoparticle Characterization

The optical properties of the synthesized Au NPs were characterized using ultraviolet–visible (UV-Vis) spectroscopy (Shimadzu UV-1800, Kyoto, Japan), with absorbance spectra recorded between 400 and 700 nm. Particle size distribution, polydispersity index, and zeta potential were analyzed with a dynamic light scattering instrument (DLS; Anton Paar LiteSizer 500, Graz, Austria). DLS determines hydrodynamic diameter and size uniformity by measuring Brownian motion, while zeta potential indicates colloidal stability by quantifying the surface charge; a higher absolute zeta potential value signifies greater electrostatic repulsion and resistance to aggregation [25]. The functional groups present on the surface of the Au NPs, which correspond to bioactive compounds from the aqueous extract involved in synthesis and stabilization, were identified using Fourier transform infrared spectroscopy (FT-IR; Bruker Alpha II, Bruker Corporation, Billerica, MA, USA) [26]. Crystallographic analysis was performed using X-ray diffraction (XRD; Malvern PANalytical X'Pert Pro, Malvern Panalytical, Malvern, Worcs, UK). The diffraction patterns provided information on phase purity and crystal structure, with crystallite size estimated via the Debye–Scherrer equation using peak broadening data (2θ and full width at half maximum values) [27]. Morphological and elemental characterization was achieved through transmission electron microscopy (TEM; Philips Tecnai 10, Philips Electron Optics B.V., Eindhoven, The Netherlands), which provides detailed visualization of nanoparticle morphology, size, and internal structure by transmitting electrons through an ultrathin sample. Elemental composition was determined using energy-dispersive X-ray spectroscopy (EDX) coupled to the TEM [26]. The specific surface area of the Au NPs was measured at 77 K under a nitrogen atmosphere employing the Brunauer–Emmett–Teller (BET; Quanta chrome Nova 1000 analyzer, Anton Paar QuantaTec Inc., Boynton Beach, FL, USA) method through adsorption–desorption isotherm analysis [28].

3. Results and Discussion

3.1. Nanoparticle Synthesis: One-Factor-at-a-Time Method

The green synthesis of Au NPs using plant extracts is a complex, multi-factor process where the final properties of the NPs—including their size, shape, stability, and optical characteristics—are governed by the intricate interplay of several reaction parameters [29–31]. These parameters, such as precursor concentration, extract concentration, reaction temperature, reaction pH, and reaction time, each exert a distinct influence on the underlying reduction kinetics, nucleation rates, and growth mechanisms [32]. A systematic study of these individual factors is therefore a critical prerequisite for understanding the process fundamentals, as it isolates and defines the specific role of each variable. The OFAT approach provides essential baseline data, revealing individual trends and identifying preliminary optimal ranges [24]. Ultimately, this foundational knowledge is indispensable for establishing robust and reproducible synthesis protocols and serves as a vital reference for any subsequent advanced multivariate optimization, such as RSM-BBD [20–22]. Table S1 presents an overview of the OFAT details.

3.1.1. Metal Precursor Concentration

The concentration of the metal precursor is a foundational parameter in nanoparticle synthesis, as it dictates the initial quantity of available metal ions for reduction and subsequent nucleation [33]. It critically influences the particle size, size distribution, and final relative SPR intensity by affecting the balance between nucleation and growth kinetics [34]. Optimizing this parameter is therefore essential to establish a baseline where the precursor is efficiently utilized without overwhelming the reducing capacity of the plant extract.

Table S1 presents the effect of varying gold precursor ($HAuCl_4$) concentrations on the synthesis of Au NPs using AKPLE, with all other parameters held constant. The data reveals a clear trend (Figure 1): increasing the $HAuCl_4$ concentration from 0.25 mM to 0.50 mM directly influenced the optical properties of the Au NPs. The SPR peak wavelength, a key indicator of nanoparticle size and shape, red-shifted from 535 nm to 556 nm. This shift suggests the formation of larger Au NPs at the higher precursor concentration. Concurrently, the absorbance intensity increased from 0.26 to 0.39, indicating a higher relative SPR intensity or concentration of NPs in the 0.50 mM sample. Significantly, $HAuCl_4$ concentrations of 0.75 mM and above showed no absorbance. This strongly implied that nanoparticle synthesis failed or was inhibited at these higher concentrations. The observed failure of nanoparticle formation at $HAuCl_4$ concentrations $\geq$ 0.75 mM likely results from a combination of factors. Primarily, the fixed quantity of bioactive compounds in the 2% (v/v) AKPLE possesses a finite reducing capacity, which becomes insufficient to effectively reduce the larger influx of gold ions, leading to incomplete reduction and potential formation of unstable, non-plasmonic clusters. Furthermore, $HAuCl_4$ is inherently acidic. Increasing its concentration in the reaction mixture is expected to lower the local pH, creating a more acidic microenvironment. As demonstrated in the pH study (Section 3.1.4), highly acidic conditions (pH 3) severely inhibit synthesis, likely due to the protonation of key functional groups (e.g., carboxylate groups) in the phytochemicals, impairing their electron-donating and capping abilities. Therefore, the inhibition at higher precursor concentrations is attributed to both the stoichiometric imbalance between metal ions and reductants and a concomitant unfavorable shift in local reaction pH.

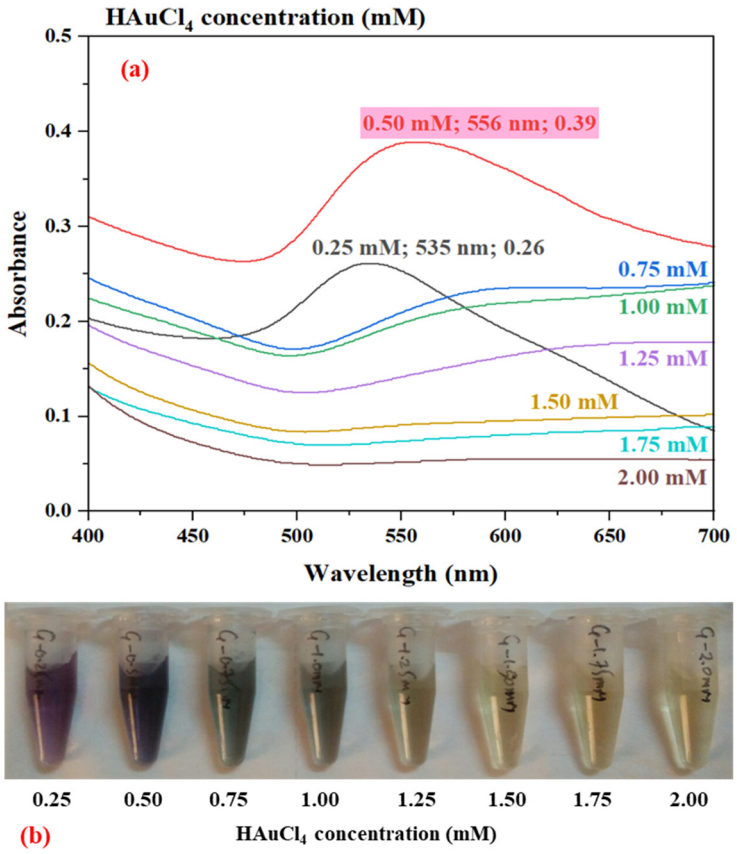


Figure 1. (**a**) UV-Vis absorption spectra and (**b**) picture of Au NP synthesis at varying $HACl_4$ concentrations (0.25, 0.50, 0.75, 1.00, 1.25, 1.50, 1.75, and 2.00 mM). All reactions were performed with a fixed AKPLE concentration of 2.0% v/v, at room temperature and a reaction pH of 6.5, for 30 min. The spectrum corresponding to the 0.50 mM $HAuCl_4$ concentration (highlighted in pink) was selected for use in subsequent experiments.

3.1.2. Extract Concentration

The concentration of a plant extract is a decisive variable in the green synthesis of NPs, as it determines the availability of reducing and capping agents in the reaction medium [35]. This parameter directly governs the nucleation rate, particle growth, and final colloidal stability, thereby influencing the size distribution, relative SPR intensity, and optical characteristics of the synthesized NPs [36]. Consequently, a systematic investigation of extract concentration is essential for identifying the optimal balance that maximizes relative SPR intensity while controlling particle dimensions.

Table S1 presents the impact of AKPLE concentration on Au NP synthesis, using a fixed $HAuCl_4$ concentration of 0.50 mM. The results demonstrated a clear threshold and subsequent optimization effect (Figure 2).

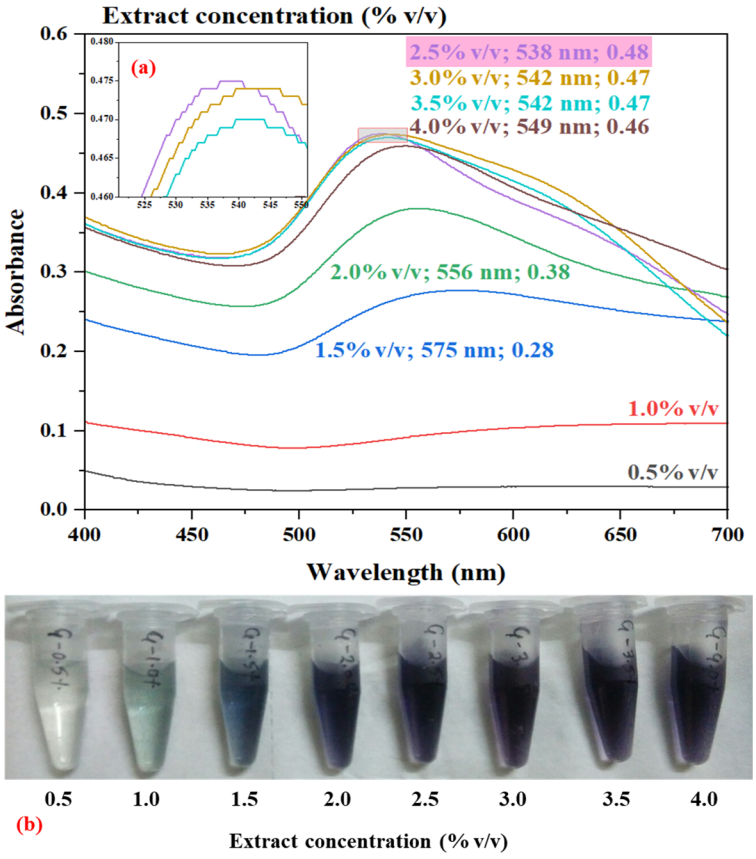


Figure 2. (**a**) UV-Vis absorption spectra and (**b**) picture of Au NP synthesis at varying AKPLE concentrations (0.5, 1.0, 1.5, 2.0, 2.5, 3.0, 3.5, and 4.0% v/v). All reactions were performed with a fixed $HAuCl_4$ concentration of 0.5 mM, at room temperature and a reaction pH of 6.5, for 30 min. The spectrum corresponding to the 2.5% v/v AKPLE concentration (highlighted in pink) was selected for use in subsequent experiments.

At low extract concentrations (0.5% and 1.0% v/v), no distinct SPR peak is observed, indicating that the concentration of bioactive reducing and capping agents is insufficient to initiate or sustain effective nanoparticle formation. Synthesis commences at an AKPLE concentration of 1.5% v/v, marked by the appearance of a broad SPR peak at 575 nm with a low absorbance of 0.28. This suggests the initial formation of larger, possibly polydisperse, Au NPs. As the extract concentration increases to 2.0% and 2.5% v/v, a significant optimization occurs: the SPR peak blue-shifts to 556 nm and then to 538 nm, indicating the production of smaller, more uniform Au NPs. Concurrently, absorbance intensifies sharply to 0.38 and 0.48, respectively, reflecting a substantial increase in relative SPR intensity. The peak at 2.5% v/v (538 nm, 0.48) likely represents an optimal balance,

where the extract provides adequate reductants and stabilizers for efficient synthesis. At higher extract concentrations (3.0% to 4.0% v/v), the system reaches a plateau. The SPR wavelength stabilizes around 542 to 549 nm, and absorbance remains high but shows a slight decrease from its peak. This suggests that beyond the optimal point, excess phytochemicals may slightly alter the capping environment or interfere with nucleation, leading to stable but marginally larger Au NPs without further relative SPR intensity enhancement. Therefore, 2.5% v/v AKPLE is identified as the most effective concentration for producing a high relative SPR intensity of relatively small Au NPs under these specific reaction conditions.

3.1.3. Reaction Temperature

Reaction temperature is a key factor in the synthesis of NPs, as it fundamentally controls the kinetic energy and reaction rates of the reduction and nucleation processes [33]. It influences the size distribution, crystallinity, and overall relative SPR intensity of NPs by modulating the activity of the plant extract's bioactive compounds [37]. Therefore, optimizing the reaction temperature is crucial for achieving efficient synthesis and obtaining NPs with desirable and consistent physicochemical properties.

Table S1 presents the impact of reaction temperature on Au NP synthesis using fixed concentrations of $HAuCl_4$ (0.50 mM) and AKPLE (2.5% v/v). The results indicated that reaction temperature significantly influences both the size and relative SPR intensity of the Au NPs (Figure 3).

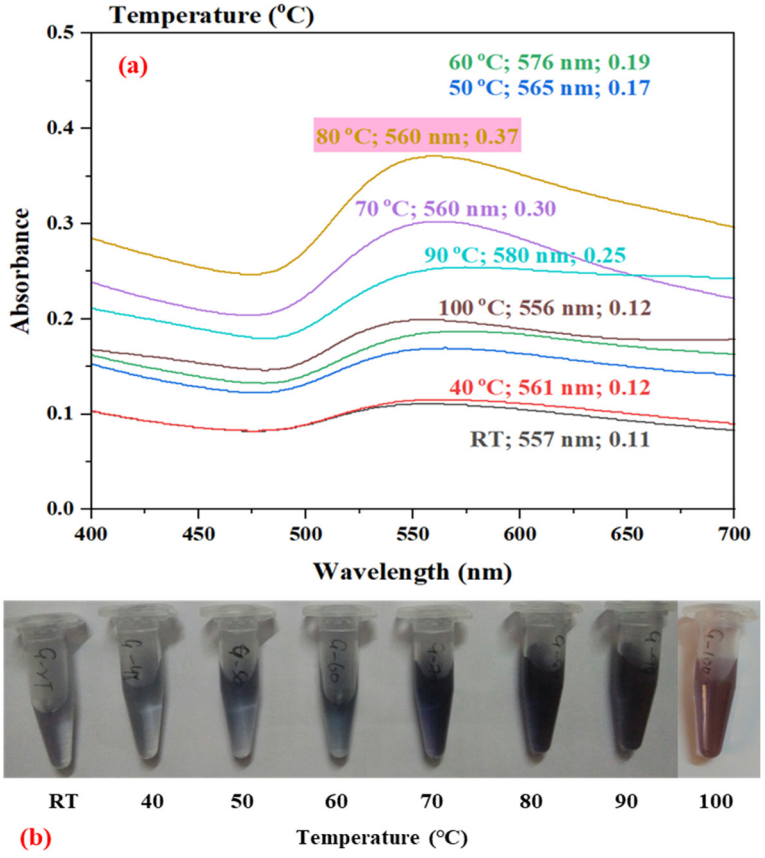


Figure 3. (**a**) UV-Vis absorption spectra and (**b**) picture of Au NP synthesis at varying reaction temperatures (room temperature, 40, 50, 60, 70, 80, 90, and 100 °C). All reactions were performed with fixed $HAuCl_4$ and AKPLE concentrations of 0.5 mM and 2.5% v/v, at a reaction pH of 6.5, for 30 min. The spectrum corresponding to the 80 °C reaction temperature (highlighted in pink) was selected for use in subsequent experiments.

A clear trend emerged, where increasing temperature generally enhances reaction kinetics, leading to a higher relative SPR intensity of Au NPs. This is evidenced by the steady rise in absorbance from 0.11 at room temperature to a maximum of 0.37 at 80 °C. The increase in absorbance correlates with a greater concentration of formed Au NPs. However, beyond 80 °C, the relative SPR intensity declines, as seen at 90 °C (0.25) and 100 °C (0.20), suggesting that excessively high temperatures may degrade the bioactive compounds in the extract or promote nanoparticle aggregation. The SPR wavelength, which indicates nanoparticle size, shows a complex relationship with temperature. The SPR peak generally red-shifts to longer wavelengths (e.g., 576 nm at 60 °C, 580 nm at 90 °C) at moderate temperatures, implying the formation of larger Au NPs, likely due to faster reduction and growth rates. Interestingly, at the optimal temperature of 80 °C, the SPR peak shifts back to 560 nm, indicating the production of smaller Au NPs alongside high relative SPR intensity, which is desirable. The subsequent blue shift at 100 °C (556 nm) alongside reduced relative SPR intensity may indicate the formation of very small particles or unstable clusters. In summary, 80 °C appears to be the optimal temperature under these conditions, striking a balance that maximizes nanoparticle relative SPR intensity while maintaining a moderately small size. Temperatures significantly above this threshold reduce efficiency, likely due to the thermal degradation of the extract's capping and reducing agents.

3.1.4. Reaction pH

The pH of the reaction medium is a fundamental parameter in the green synthesis of NPs, as it significantly influences the ionization state and chemical reactivity of the phytochemicals responsible for reduction and stabilization [38]. It determines the surface charge of the developing NPs, thereby affecting their nucleation kinetics, growth, colloidal stability, and final optical properties [39]. Consequently, investigating the effect of pH is essential for identifying the optimal window where the plant extract's bioactive compounds function most effectively to produce uniform and stable NPs.

Table S1 presents the effect of reaction pH on Au NP synthesis using optimized concentrations of $HAuCl_4$ (0.50 mM) and AKPLE (2.5% v/v) at 80 °C. The results reveal a strong dependence of nanoparticle formation on the reaction pH, affecting both size and relative SPR intensity (Figure 4). At highly acidic conditions (pH 3), synthesis is markedly inefficient. The SPR peak is broad and red-shifted to 582 nm, indicating the formation of large, aggregated, or irregular particles. The very low absorbance (0.11) confirms a poor relative SPR intensity, likely because the acidic environment protonates the functional groups in the plant extract, impairing their ability to reduce gold ions and stabilize the Au NPs. Optimal synthesis occurs in a broad near-neutral to mildly alkaline range from pH 5 to 9. The SPR peak stabilizes between 556 nm and 561 nm, signifying the consistent production of moderately sized Au NPs. Most importantly, the absorbance values in this range are high and stable (0.35), demonstrating maximum relative SPR intensity. This pH window provides ideal conditions for the deprotonation of the extract's bioactive compounds, enhancing their reducing and capping capabilities. At strongly alkaline pH 11, synthesis is again suboptimal. While the SPR peak blue-shifts significantly to 529 nm, suggesting the formation of very small NPs, the absorbance drops sharply to 0.19. This indicates a much lower relative SPR intensity. The high alkalinity may alter or degrade the phytochemicals in the extract or cause overly rapid nucleation that leads to incomplete growth and instability. In conclusion, pH 5 is optimal for this green synthesis method, maximizing relative SPR intensity and producing Au NPs of consistent size.

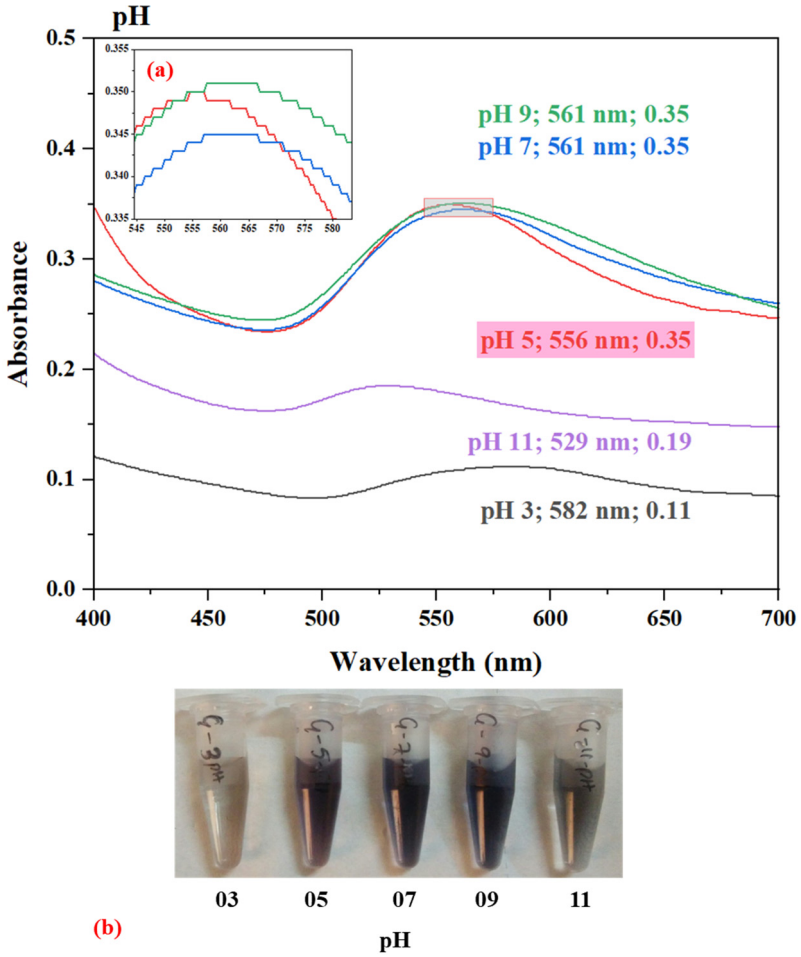


Figure 4. (**a**) UV-Vis absorption spectra and (**b**) picture of Au NP synthesis at varying reaction pH values (3, 5, 7, 9, and 11). All reactions were performed with fixed $HAuCl_4$ and AKPLE concentrations of 0.5 mM and 2.5% v/v, at a reaction temperature of 80 °C, for 30 min. The spectrum corresponding to the reaction pH of 5 (highlighted in pink) was selected for use in subsequent experiments.

3.1.5. Reaction Time

Reaction time is a critical parameter in green nanoparticle synthesis, as it directly governs the kinetics of nucleation, growth, and maturation, which ultimately determine the final particle size, uniformity, and relative SPR intensity [36]. Controlling the reaction time is essential to achieve complete reduction of the metal precursor while preventing overgrowth or destabilization of NPs, such as aggregation or degradation of the capping agents [40]. Therefore, systematically studying the influence of reaction time provides key insights for optimizing the synthesis process to obtain stable NPs with desirable optical and physicochemical properties.

Table S1 presents the effect of reaction time on Au NP synthesis under optimized conditions of $HAuCl_4$ concentration (0.50 mM), AKPLE (2.5% v/v), temperature (80 °C), and pH (5). The results demonstrated a clear progression in nanoparticle formation and stability over time (Figure 5). At time 0, no SPR peak is observed, confirming that no NPs have formed prior to the reaction's initiation. After 30 min, a distinct SPR peak emerges at 564 nm with an absorbance of 0.27, indicating the successful nucleation and initial growth of Au NPs. The peak position suggests the formation of Au NPs of moderate size. The most significant development occurs at 60 min. The SPR peak blue-shifts to 548 nm, signaling the production of smaller, more uniform NPs, likely due to Ostwald ripening or focused growth. Concurrently, the absorbance increases sharply to 0.43, representing the highest relative SPR intensity observed. This indicates that 60 min is sufficient for near-complete

reduction of the Au precursor and effective stabilization by the phytochemicals. Extending the reaction time to 90 and 120 min results in a plateau and then a decline in performance. The SPR peak red-shifts slightly to 552 nm and 558 nm, suggesting a mild increase in particle size or aggregation over prolonged heating. More importantly, the absorbance decreases to 0.42 and 0.36, respectively.

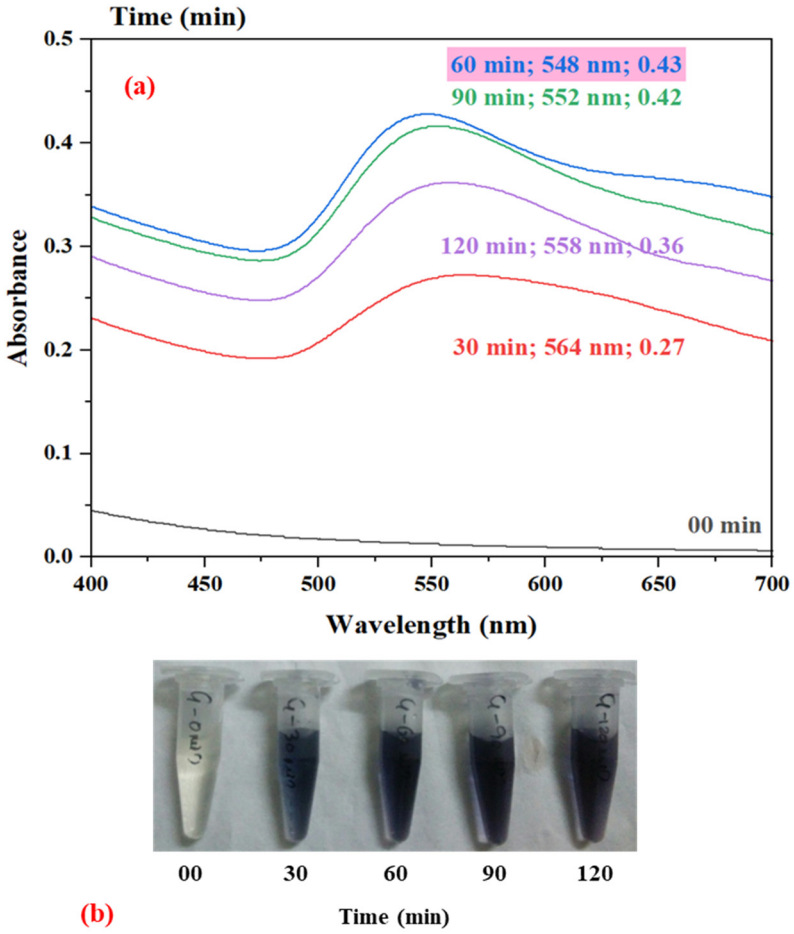


Figure 5. (**a**) UV-Vis absorption spectra and (**b**) picture of Au NP synthesis at varying reaction times (0, 30, 60, 90, and 120 min). All reactions were performed with fixed $HAuCl_4$ and AKPLE concentrations of 0.5 mM and 2.5% v/v, at a reaction temperature of 80 °C and a reaction pH of 5. The spectrum corresponding to the reaction time of 60 min (highlighted in pink) was selected for use in subsequent experiments.

It is important to note that beyond the position and intensity of the SPR peak, the baseline elevation observed in the UV-Vis spectra provides additional insight into the colloidal state of the Au NPs. A rising baseline, particularly in the longer wavelength region (>600 nm), is characteristic of increased light scattering, which typically arises from the presence of larger particles or the formation of aggregates [41]. In the present study, the gradual baseline rise observed with increasing reaction time—especially at 90 and 120 min—suggests a progressive aggregation of the Au NPs, rather than simply continued nanoparticle formation. This interpretation is further supported by the connected red shift of the SPR peak (from 548 nm at 60 min to 558 nm at 120 min), which indicates either an increase in primary particle size or, more likely, the onset of interparticle coupling due to aggregation [41]. The color change of the colloidal solutions (Figure 5b), shifting from a stable ruby red toward a purplish-gray hue at extended reaction times, visually corroborates this aggregation behavior. Thus, while the appearance of a distinct SPR peak confirms successful nanoparticle synthesis, the combination of baseline elevation, peak

red-shifting, and visual observation collectively indicates that the colloidal stability of the system is time-dependent. Optimal synthesis conditions must therefore balance maximum relative SPR intensity (as indicated by peak absorbance) against the maintenance of colloidal stability (as indicated by minimal baseline rise and controlled SPR peak position). This dual consideration reinforces the importance of selecting 60 min as the optimal reaction time, where absorbance is maximized while aggregation indicators remain minimal.

The OFAT analysis identified a set of optimal synthesis conditions for producing stable Au NPs using the AKPLE. This protocol utilized a metal precursor ($HAuCl_4$) concentration of 0.50 mM combined with a plant extract concentration of 2.5% (v/v). The reaction was carried out at 80 °C and a pH of 5 for a duration of 60 min. Under these specific parameters, the synthesis achieves maximum relative SPR intensity, as reflected by the highest recorded absorbance values, while simultaneously promoting the formation of moderately sized and colloidally stable particles, as indicated by the characteristic SPR peak. Table S2 presents a comparison with a few studies reported in the literature.

3.2. Nanoparticle Synthesis: Statistical Optimization

The successful modeling and optimization presented here highlighted the advantage of a systematic multivariate approach over conventional strategies. Commonly reported OFAT studies on plant-mediated Au NP synthesis, while valuable for establishing baseline trends, are constrained to exploring 1D parameter spaces [11,12,14,18]. This often leads to a fragmented understanding and conditions that are optimal in isolation but not in combination. Even when RSM is employed, analyses are often limited to fewer variables or a single response objective, such as maximizing absorbance [20–23]. In contrast, this study utilized a five-factor BBD to model strong nonlinear curvatures and employed a desirability function to explicitly reconcile two conflicting optical responses: SPR peak position (λ_{max}) and its intensity. This dual objective—minimizing λ_{max} to promote smaller, well-dispersed particles while simultaneously maximizing absorbance to ensure high plasmonic absorbance—represents a more application-relevant optimization goal.

3.2.1. Experimental Responses and Variability Across the Design Space

The five-factor BBD (Table S3) generated measurable and systematic variation in both UV–Vis responses, confirming that the selected factor ranges were sufficiently broad to capture response curvature and to support optimization. Across the 46 runs, the SPR peak position (λ_{max}) spanned from 528 to 571 nm, with a mean of 549 ± 11 nm, while the absorbance at the SPR maximum (absorbance at λ_{max}) ranged from 0.35 to 0.61, with a mean of 0.49 ± 0.07 (Table 1). The fact that both responses varied appreciably without requiring data transformation indicates that the measurement scale was appropriate and that the design space captured meaningful changes in NP optical behavior, including both peak-position shifts and changes in peak intensity that are relevant to NP synthesis control.

Table 1. Summary statistics for experimental responses (n = 46).

Response	Description	Units	Minimum	Maximum	Mean	Standard Deviation	Transform	Selected Model
R1	λ_{max} (SPR peak position)	nm	528	571	549	11	None	Quadratic
R2	Absorbance at λ_{max} (SPR intensity)	-	0.35	0.61	0.49	0.07	None	Quadratic

3.2.2. Model Selection and Justification of the Quadratic Form

Model selection for each response was guided by Design-Expert fit summary criteria, including sequential sum of squares, lack-of-fit testing, and predictive statistics. For

both λ_{max} and absorbance at λ_{max}, the quadratic model was selected because inclusion of quadratic terms produced a statistically significant improvement over lower-order models (sequential $p < 0.0001$), while the cubic model was aliased within the BBD structure and therefore not interpretable. Importantly, the selected quadratic models exhibited a non-significant lack of fit relative to pure error estimated from the replicated center points (Table 2), indicating that the quadratic surfaces adequately represented the response behavior within the explored domain and that remaining residual variation was consistent with experimental noise rather than systematic model misspecification.

Table 2. Fit summary for R1 (λ_{max}) and R2 (absorbance at λ_{max}).

Response	Model	Sequential *p*-Value	Lack of Fit *p*-Value	Adjusted R^2	Predicted R^2	Decision
R1	Linear	<0.0001	0.18	0.77	0.76	Not selected
	2FI	0.9976	0.11	0.71	0.69	Not selected
	Quadratic	<0.0001	0.96	0.95	0.92	Selected
	Cubic	0.9994	0.51	0.89	0.24	Aliased
R2	Linear	<0.0001	0.36	0.70	0.70	Not selected
	2FI	1.0000	0.22	0.61	0.61	Not selected
	Quadratic	<0.0001	1.00	0.94	0.94	Selected
	Linear	<0.0001	0.36	0.70	0.70	Not selected

3.2.3. Model Adequacy, Goodness of Fit, and Predictive Capability

The fitted quadratic models demonstrated strong explanatory power and robust predictive performance (Table 3). For λ_{max}, the model yielded $R^2 = 0.97$, adjusted $R^2 = 0.95$, and predicted $R^2 = 0.92$, with a low residual standard deviation of 2.62 nm and adequate precision of 22.66. These metrics indicate that the model explains the majority of response variance, maintains strong adjusted fit after accounting for the number of terms, and retains high predictive capability within the design space. For absorbance at λ_{max}, the quadratic model likewise achieved $R^2 = 0.97$, adjusted $R^2 = 0.94$ and predicted $R^2 = 0.94$, with a residual standard deviation of 0.02 and adequate precision of 23.14. For both responses, the difference between adjusted R^2 and predicted R^2 remained well below the commonly used threshold of 0.2, supporting good generalization and indicating that the models were not overfitted. Collectively, these adequacy statistics confirm that both response surfaces were suitable for the interpretation of factor effects and for optimization within the experimental region.

Table 3. Model adequacy statistics for the selected quadratic models.

Response	Standard Deviation	R^2	Adjusted R^2	Predicted R^2	Coefficient of Variation (%)	Adequate Precision
R1: λ_{max} (nm)	2.62	0.97	0.95	0.91	0.48	22.66
R2: Absorbance at λ_{max}	0.02	0.97	0.94	0.94	3.34	23.14

3.2.4. Model Diagnostic Validation Using Predicted vs. Actual and Influence Statistics

The data points cluster closely around the 45° line (Figure 6a) across the full λ_{max} range (528 to 571 nm), indicating that the fitted quadratic model reproduces the observed SPR peak positions with high accuracy and without a visible systematic tendency to over- or under-predict at either end of the response. This visual fit is consistent with the diagnostic statistics, where the residuals (actual − predicted) remain small relative to the total response span and are balanced in sign; the largest deviations are modest (approximately +4.9 and +4.2 nm on the positive side and −3.8 nm on the negative side). The externally studentized residuals remain within about ±2.2, supporting the absence of

severe outliers within the modeled domain. The leverage distribution follows the expected Box–Behnken structure, with higher leverage at design-edge points (≈0.5) and lower leverage at replicated center points (≈0.17), indicating that both boundary information and pure-error estimation are appropriately represented. Although a few observations show comparatively larger DFFITS values, Cook's distances remain low (well below 1), confirming that no single run disproportionately governs the fitted surface. Collectively, the agreement in this plot and the accompanying diagnostics supports the use of the quadratic model for λ_{max} to interpret factor effects and to conduct optimization within the investigated ranges.

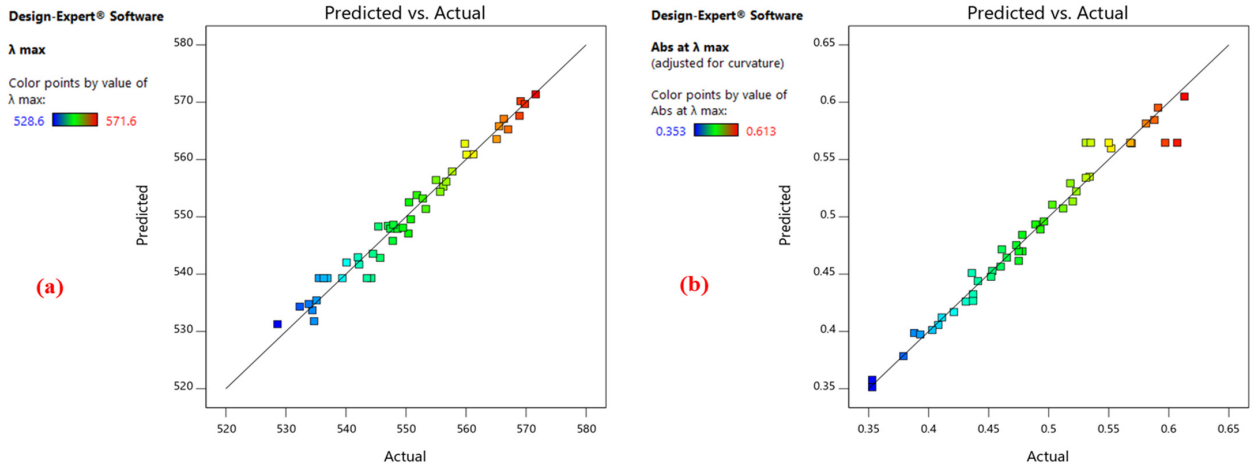


Figure 6. (**a**) Predicted vs. actual plot for the SPR peak position (λ_{max}, nm) obtained from the quadratic RSM model. Predicted vs actual scatter plot comparing experimentally measured λ_{max} (nm) with quadratic model predictions; the 45° reference line represents perfect agreement, and the point color encodes the λ_{max} magnitude across the design space. (**b**) Predicted vs. actual plot for absorbance at the SPR maximum (absorbance at λ_{max}) obtained from the quadratic RSM model. Predicted vs actual scatter plot comparing experimentally measured absorbance at λ_{max} with quadratic model predictions; the 45° reference line represents perfect agreement, and the point color encodes the absorbance magnitude across the design space.

The predicted vs actual relationship shows (Figure 6b) near-linear alignment across the full absorbance range (0.35 to 0.61), demonstrating that the quadratic model captures the dominant structure of the SPR intensity response without an apparent systematic bias at low and mid absorbance levels. Most observations exhibit small residuals (typically on the order of 0.00 to 0.01), while a small subset deviates more visibly from the 45° line, consistent with the larger residuals in the diagnostics. The most pronounced deviation occurs for Run 23 (actual 0.61 vs. predicted 0.56; residual +0.04), which is reflected by an externally studentized residual of 3.41, marking it as statistically unusual relative to the model's expected error. Notably, this point has low leverage (0.17), characteristic of center-point replicates, and the center-point set shows both positive and negative departures from the same predicted value (e.g., residuals around −0.03, −0.03, +0.03, and +0.04), indicating appreciable pure-error/measurement scatter at the center rather than a consistent model bias. Influence diagnostics remain modest overall, with Cook's distances well below 1 and leverage behaving as expected for the design, indicating that the fitted surface is not being driven by a small number of influential observations. Taken together, the plot and diagnostics support the adequacy of the quadratic model for absorbance at λ_{max} for interpretation and optimization within the explored experimental domain, while transparently indicating that center-point variability contributes meaningfully to the residual spread.

3.2.5. ANOVA Interpretation and Significance Structure of the Fitted Surfaces

ANOVA confirmed that both quadratic models were statistically significant and that the fitted response surfaces were appropriate representations of the experimental data (Table 4). For λ_{max}, the overall model was highly significant ($F = 42.16$, $p < 0.0001$) and the lack-of-fit term was non-significant ($p = 0.9558$), demonstrating that residual deviation from the model was comparable to pure experimental error derived from center-point replication. All five linear main effects (A: $HAuCl_4$ concentration, B: AKPLE concentration, C: temperature, D: pH, and E: time) were significant ($p < 0.0001$), confirming that each synthesis variable contributed materially to the SPR peak position. In addition, all quadratic terms (A^2 to E^2) were significant, including C^2 ($p = 0.0006$) and the remaining squared terms ($p < 0.0001$), demonstrating pronounced curvature and indicating that λ_{max} does not change monotonically across the investigated ranges. In contrast, the two-factor interaction terms were not significant at the 0.05 level, implying that within the tested region λ_{max} was governed primarily by additive main effects and curvature rather than strong pairwise synergies. Two interactions (CE and DE) exhibited weak trends but did not reach significance ($p = 0.0705$ and 0.0881) and, therefore, should be interpreted cautiously.

Table 4. Key ANOVA outcomes for the quadratic model.

Response	Metric/Term Group	Result
R1 (λ_{max})	Model significance	$F = 42.16$, $p < 0.0001$ (significant)
	Lack of fit	$F = 0.3556$, $p = 0.9558$ (not significant)
	Significant linear terms	A, B, C, D, E (all $p < 0.0001$)
	Significant quadratic terms	A^2, B^2, C^2 ($p = 0.0006$), D^2, E^2 (all $p < 0.0001$)
	Interaction terms	All non-significant ($p > 0.05$); CE and DE show weak trends ($p = 0.0705$; 0.0881)
R2 (absorbance at λ_{max})	Model significance	$F = 39.35$, $p < 0.0001$ (significant)
	Lack of fit	$F = 0.0741$, $p = 1.0000$ (not significant)
	Significant linear terms	A ($p < 0.0001$), B ($p < 0.0001$), C ($p = 0.0001$), D ($p = 0.0021$), E ($p < 0.0001$)
	Significant quadratic terms	A^2, B^2, C^2, D^2, E^2 (all $p < 0.0001$)
	Interaction terms	All non-significant ($p > 0.05$)

For absorbance at λ_{max}, the overall model was similarly significant ($F = 39.35$, $p < 0.0001$), with a non-significant lack of fit ($p = 1.0000$), again indicating that the quadratic form adequately captured response behavior. All five linear terms were significant ($p \leq 0.0021$), and all squared terms were highly significant ($p < 0.0001$), indicating strong nonlinearity and the presence of interior optima rather than purely increasing or decreasing trends. As with λ_{max}, interaction terms were not significant, supporting the conclusion that within the explored region, the response is largely driven by individual-factor contributions and quadratic curvature. A key quantitative outcome of the ANOVA for absorbance at λ_{max} was the dominance of the AKPLE concentration main effect (factor B), which exhibited a very large F-value ($F = 490.85$), identifying extract concentration as the most influential lever controlling SPR intensity across the design space.

3.2.6. Final Regression Models in Coded Form and Implications of Coefficient Signs

The final regression models in coded factors are given in Equations (2) and (3). The coded form is preferred for interpretation because the coefficients are on a comparable scale

across all factors, allowing direct comparison of the relative direction and strength of each effect within the experimental domain.

$$\begin{aligned}\lambda_{max} = 539.30 + 10.19A - 6.19B + 6.55C + 3.81D + 9.86E + 0.85AB - 1.10AC \\ + 0.60AD - 0.775AE + 0.05BC + 0.10BD + 0.925BE + 0.675CD + 2.47CE \\ + 2.33DE + 6.84A^2 + 5.43B^2 + 3.49C^2 + 8.94D^2 + 5.95E^2\end{aligned} \quad (2)$$

$$\begin{aligned}\text{Absorbance at } \lambda_{max} = 0.5647 + 0.0252A + 0.0899B + 0.0185C + 0.0139D \\ + 0.0235E - 0.0020AB + 0.0033AC + 0.0095AD - 0.0010AE - 0.0008BC \\ + 0.0065BD + 0.0017BE + 0.0040CD + 0.0010CE - 0.0047DE - 0.0587A^2 \\ - 0.0376B^2 - 0.0395C^2 - 0.0324D^2 - 0.0576E^2\end{aligned} \quad (3)$$

In Equation (2), the positive linear coefficients for A ($HAuCl_4$ concentration), C (temperature), D (pH), and E (time) indicate that, within the linear component of the model, increasing these factors shifts the SPR maximum to longer wavelengths (red shift), whereas the negative linear coefficient for B (AKPLE concentration) indicates that increasing extract concentration shifts λ_{max} toward shorter wavelengths (blue shift). The positive squared terms in Equation (2) indicate convex curvature in the response surface, implying that λ_{max} is characterized by turning behavior within the design space rather than being described adequately by straight-line trends; practically, this means that minima in λ_{max} can occur at interior factor settings depending on the combined balance of linear and quadratic contributions.

In Equation (3), all linear coefficients are positive, indicating that each factor contributes positively to the absorbance at the SPR maximum in the linear component of the fitted surface. However, all quadratic coefficients in Equation (3) are negative, demonstrating concave-down curvature and therefore an internal optimum for absorbance at λ_{max} within the studied ranges, rather than continuous improvement at the highest factor levels. Finally, the relatively small magnitudes of the interaction coefficients in Equations (2) and (3), together with the ANOVA finding that interaction terms were statistically non-significant, support the inference that optimization is governed mainly by balancing the principal effects and curvature of individual factors, rather than by exploiting narrow, interaction-driven operating windows.

3.2.7. Effects on R1 (λ_{max}): Response Trends and Interpretation from Interaction Plots

The interaction plots for λ_{max} (Figures S1–S3) consistently show that $HAuCl_4$ concentration and reaction time are major drivers of SPR peak position, with temperature and pH providing additional upward shifts. In the A-based plots (Figure S1), λ_{max} increases strongly as $HAuCl_4$ rises from 0.25 to 0.75 mM, indicating a systematic red shift with increasing precursor concentration under otherwise fixed conditions. This behavior is consistent with the large positive A coefficient and the significant A^2 term, and it implies that excessive precursor concentration promotes conditions associated with longer-wavelength SPR maxima within the explored system. Simultaneously, λ_{max} shifts upward with longer reaction time, as seen in the A to E and pH–time slices, consistent with the strong positive E coefficient and significant E^2 term. The time effect indicates that peak position continues to evolve during the studied reaction window, which is consistent with ongoing changes in the nanoparticle population as the reaction proceeds.

Across B-based plots (Figure S2), AKPLE concentration exhibits a characteristic curvilinear effect on λ_{max}, with the lowest λ_{max} values typically occurring around intermediate extract levels (approximately near the design-center region) and slightly higher λ_{max} toward the low and high ends of the extract range. This U-shaped behavior is consistent with the negative linear B coefficient combined with a positive B^2 term, indicating that

increasing extract concentration initially promotes conditions that shift λ_{max} toward shorter wavelengths, but beyond an intermediate region, the peak position can shift back upward. Importantly, in most two-factor slices, the curves for high vs. low levels of the second factor remain approximately parallel, visually reinforcing the ANOVA conclusion that two-factor interactions are weak and that peak-position behavior is dominated by main effects and curvature.

The temperature–pH and temperature–time slices (Figure S3) further show that increasing temperature and increasing pH generally shift λ_{max} to longer wavelengths, with the lowest λ_{max} values typically occurring nearer to moderate temperature and near-neutral pH. The pH effect is notably curved, with λ_{max} often exhibiting a minimum around the neutral range and increasing toward both acidic and alkaline extremes, consistent with a strong D^2 term. Overall, the λ_{max} plots support the practical conclusion that lower λ_{max} values are favored by moderate precursor concentration, sufficiently high extract concentration, controlled temperature, near-neutral pH, and avoidance of unnecessarily prolonged reaction time, subject to simultaneous consideration of SPR intensity.

3.2.8. Effects on R2 (Absorbance at λ_{max}): Response Trends and Interpretation from Interaction Plots

The interaction plots for absorbance at λ_{max} (Figures S4–S6) show a distinctly different response structure compared with λ_{max}. Across plots involving $HAuCl_4$ concentration (Figure S4), absorbance exhibits a consistent concave-down dependence on precursor concentration, increasing from low precursor levels to a mid-range maximum and then decreasing slightly toward the highest precursor concentration. This is the clearest visual manifestation of the large negative A^2 coefficient in the absorbance model and indicates that peak intensity is maximized at an intermediate precursor concentration rather than at the upper bound. This behavior is practically important because it shows that higher precursor loading does not necessarily translate to stronger SPR intensity, likely because conditions at very high precursor levels can shift the system away from the optical optimum (for example, by altering particle population characteristics and increasing scattering contributions that reduce the peak height at λ_{max}).

The dominant role of AKPLE concentration is evident across the B-based plots (Figure S5), where absorbance increases strongly with extract concentration across most of the studied range and begins to level off as the system approaches the upper extract bound. This pattern is consistent with the very large positive B coefficient combined with the negative B^2 term, indicating strong gains followed by diminishing returns at high extract concentration. Temperature, pH, and time generally provide additional positive shifts in absorbance but with smaller magnitude than the extract effect, aligning with the comparatively smaller linear coefficients for C, D, and E. The temperature and pH slices (Figure S6) exhibit broad optima, often around moderate-to-high temperature and near-neutral to mildly alkaline pH, consistent with the negative C^2 and D^2 coefficients and the presence of interior maxima.

As with λ_{max}, the general parallelism of curves across two-level slices supports the ANOVA finding that interaction terms do not materially govern absorbance at λ_{max} within the studied region. Consequently, absorbance optimization is best approached through balancing main effect magnitudes with quadratic curvature, rather than relying on specific interacting factor pairs.

3.2.9. 3D Response Surfaces and Identification of Favorable Regions

Across the 3D response surfaces for λ_{max} (Figures S7a–S16a) and absorbance at λ_{max} (Figures S7b–S16b), the fitted quadratic models delineate coherent 'favorable regions' in the experimental domain and, importantly, indicate that response control is driven

predominantly by the main effects with pronounced quadratic curvature rather than by strong pairwise synergies. The contour projections are generally smooth and only weakly rotated, and where experimental design points are overlaid, they follow the predicted surfaces without obvious systematic deviation, which supports the interpretation that the models capture the dominant curvature needed for process navigation within the Box–Behnken bounds.

For λ_{max}, the surfaces consistently identify $HAuCl_4$ concentration (A) as the strongest red-shifting driver, with λ_{max} increasing across essentially every plane as precursor loading moves from the low to high end of the range. Temperature (C) and reaction time (E) also act as red-shifting levers, with curvature indicating that their influence is not strictly linear across 70 to 90 °C and 30 to 90 min, respectively; in practical terms, higher temperature and longer time move the plasmon maximum toward longer wavelengths, consistent with continued evolution of the particle population during the reaction window. In contrast, AKPLE concentration (B) generally counteracts red shifting by pushing λ_{max} toward shorter wavelengths, and its effect shows saturation-type curvature at the upper end, implying diminishing incremental benefit once a sufficiently strong reducing/capping environment is established. pH (D) behaves as a curvature-dominant variable that positions an interior minimum rather than enforcing a monotonic shift, with the lowest λ_{max} consistently centered around slightly acidic to near-neutral conditions and higher λ_{max} emerging toward both acidic and alkaline extremes, particularly on the alkaline side. When these patterns are integrated, the most robust low-λ_{max} region is concentrated at low-to-moderate precursor loading combined with moderate-to-high AKPLE concentration, operated at lower-to-moderate temperatures, near-neutral pH, and shorter reaction times, indicating that λ_{max} minimization is achieved by simultaneously restraining growth-promoting drivers (A, C, E) while maintaining sufficient extract-mediated reduction and stabilization (B) under an interior pH window.

For absorbance at λ_{max}, the surfaces uniformly show an interior maximum across all examined factor planes, reflecting the 'rise-then-roll-off' behavior expected for a response governed by positive linear effects with concave-down quadratic terms. AKPLE concentration (B) remains the dominant positive lever for strengthening SPR intensity, with absorbance rising sharply from low extract levels and then displaying curvature consistent with saturation at the upper end of the studied range. $HAuCl_4$ concentration (A) exhibits a clear optimum in the mid-range rather than at the high boundary, indicating that excessive precursor loading does not continue to increase peak intensity under fixed extract and temperature conditions and can instead reduce the net absorbance at the SPR maximum. Temperature (C) and reaction time (E) also show windowed optima, where mid–high temperatures and intermediate-to-long times enhance absorbance up to a maximum region but do not show proportional gains at the highest settings, consistent with a shift from productive nanoparticle formation toward regimes that do not further increase the optical density at the plasmon maximum. pH (D) again operates mainly through an interior optimum, with absorbance highest around near-neutral conditions and reduced toward acidic and alkaline extremes, indicating that peak development is most effective within a pH window that supports favorable extract functionality for reduction and capping. Collectively, these surfaces place the high-absorbance region in a practical operating band characterized by moderate precursor concentration, moderate-to-high AKPLE concentration, near-neutral pH, and mid–high temperature with intermediate reaction time.

When λ_{max} minimization and absorbance maximization are considered together, the combined surfaces highlight a structured trade-space rather than conflicting, disjoint optima: λ_{max} generally benefits from restrained precursor loading, lower temperatures, and shorter times, whereas absorbance at λ_{max} requires sufficient precursor to build intensity but

still favors an intermediate optimum rather than the high-A boundary, with both responses agreeing on the value of moderate-to-high AKPLE concentration and near-neutral pH. Accordingly, the response surfaces in this section provide the mechanistic and statistical basis for the multi-response desirability optimization presented next, because they visually and quantitatively justify that the best operating region is expected to lie in an interior zone defined by moderate A, moderate-to-high B, near-neutral D, and controlled C and E, rather than at any single extreme of the experimental ranges.

3.2.10. Multi-Response Numerical Optimization and Optimal Operating Conditions

Because λ_{max} and absorbance at λ_{max} capture complementary aspects of NP optical behavior, optimization was treated as a simultaneous multi-response problem rather than a single-response maximization. Numerical optimization using the desirability function identified operating conditions that jointly minimize λ_{max} while maximizing absorbance at λ_{max} within the experimental bounds. The best-ranked solution returned by the software achieved an overall desirability of 1.000 (solution 1 of 100), indicating that the selected factor combination most effectively satisfied the defined goals within the fitted response surfaces.

At the predicted optimal conditions of $HAuCl_4$ = 0.44 mM, AKPLE = 3.50% (*v*/*v*), temperature = 80.6 °C, pH = 7.2, and reaction time = 66.7 min, the models predict λ_{max} = 540 nm and absorbance at λ_{max} = 0.61. (Table 5 and Figure S17). This solution is consistent with the response-surface trends: a moderate precursor concentration supports strong plasmonic intensity without pushing the system toward excessive red shifting, while an extract concentration near the upper bound strongly enhances absorbance and favors a lower λ_{max} through improved reduction and stabilization capacity. The predicted temperature and pH lie close to the design-center region, consistent with the broad optima and curvature observed in the corresponding surfaces, while the predicted time lies modestly above the center point, indicating that sufficient reaction duration is beneficial for intensity but should remain controlled to limit red shifting.

Table 5. Numerical optimization and experimental validation results for Au NPs.

Category	Parameter	Value
Optimized synthesis conditions (RSM)	$HauCl_4$ concentration (mM)	0.44
	AKPLE concentration (*v*/*v*)	3.50
	Temperature (°C)	80.6
	pH	7.2
	Time (min)	66.7
SPR response	Predicted λ_{max} (nm)	540
	Experimental λ_{max} (nm)	540
	Prediction error (%)	0.00
	Predicted absorbance at λ_{max}	0.61
	Experimental absorbance at λ_{max}	0.61
	Prediction error (%)	0.16
Model adequacy	Overall desirability	1.000

Overall, the RSM analysis confirms that the synthesis variables significantly influence both SPR peak position and intensity, with strong curvature in both responses and minimal dependence on pairwise interactions within the explored factor ranges. The fitted quadratic models therefore provide a statistically validated basis for selecting synthesis conditions that deliver an intense SPR band while maintaining a controlled, lower λ_{max} consistent with improved NP dispersion and optical quality, and the desirability-based solution provides a practical operating point for experimental confirmation. Table S4 presents a few examples reported in the literature on the application of RSM for Au NP synthesis.

3.3. Nanoparticle Characterization

Comprehensive physicochemical characterization is essential to validate the success of the statistical optimization and to confirm the formation of well-defined Au NPs. It provides critical information on the Au NPs' size, morphology, crystalline structure, surface chemistry, and colloidal stability, which are the ultimate metrics for assessing synthesis efficacy. This characterization bridges the gap between predicted optical properties from RSM models and the actual structural and functional attributes of the synthesized NPs.

3.3.1. Hydrodynamic Diameter

The hydrodynamic diameter of the synthesized Au NPs was determined using DLS analysis. The particle size distribution curve (Figure 7) indicates a predominantly monomodal profile, with a hydrodynamic diameter ranging from approximately 50 to 350 nm. The calculated average particle size was 142.56 nm, accompanied by a polydispersity index of 0.256, signifying a moderately broad but acceptable size distribution. This polydispersity index value reflects a relatively stable colloidal system without severe aggregation, though some polydispersity is present, which is typical of green-synthesized NPs. The observed hydrodynamic size is larger than the corresponding TEM-derived core size, which is expected as DLS measures the hydrated particle diameter, including the capping layer and solvation shell formed by the phytochemicals from the *K. pinnata* extract [42,43].

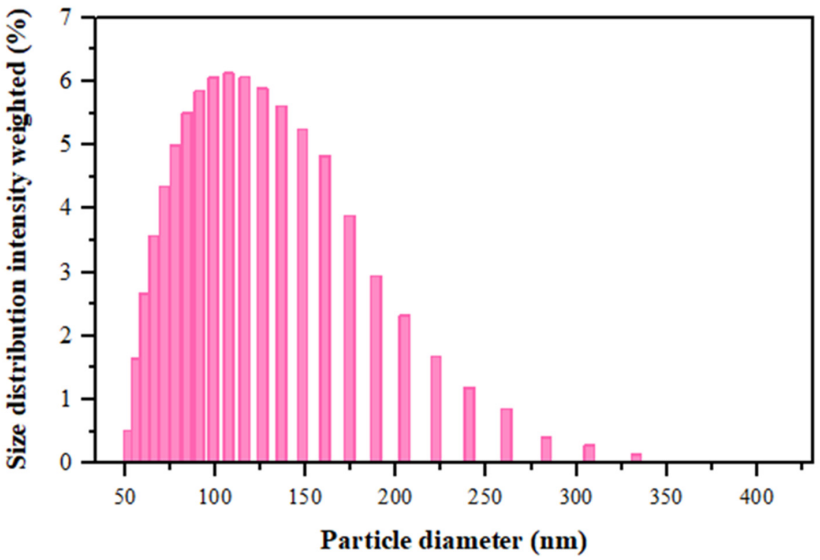


Figure 7. DLS spectra of Au NPs.

3.3.2. Zeta Potential

The colloidal stability of the synthesized Au NPs was evaluated by zeta potential measurements. As shown in Figure 8, the Au NPs exhibited a zeta potential of −30.45 mV, indicating a strong negative surface charge. This value exceeds the ±30 mV threshold typically associated with good electrostatic stabilization [44], suggesting the formation of a colloidally stable suspension. The negative charge is commonly attributed to the adsorption of anionic phytochemicals from the *K. pinnata* leaf extract onto the nanoparticle surface during synthesis. While FT-IR analysis (Section 3.3.3) confirms the presence of hydroxyl and carbonyl functional groups characteristic of such biomolecules, it is important to note that this attribution remains a proposed mechanism based on indirect evidence. Without direct comparative controls—such as Au NPs synthesized via a chemical route or measurement of the extract's intrinsic zeta potential—the contribution of other factors, including the intrinsic charge of the gold core or the adsorption of ions from the aqueous

medium, cannot be definitively excluded. Nevertheless, the magnitude of the zeta potential confirms excellent electrostatic stabilization, which prevents aggregation through strong interparticle repulsion.

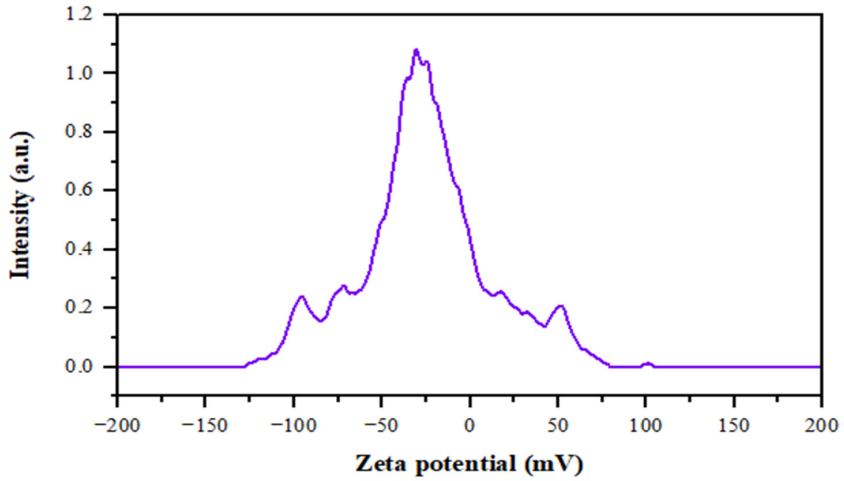


Figure 8. Zeta potential of Au NPs.

3.3.3. Functional Groups

FT-IR spectroscopy was employed to identify the functional groups from the *K. pinnata* leaf extract involved in the reduction of gold ions and the stabilization of the synthesized Au NPs. The FT-IR spectrum of the purified Au NPs (Figure 9) was analyzed, revealing a complex adsorption profile of biomolecules on the nanoparticle surface [45]. The spectrum is dominated by two key features. First, a very strong, very broad absorption band spanning 3200 to 3400 cm^{-1} is definitive for O–H stretching vibrations, characteristic of alcohols and phenols. The broadness indicates extensive hydrogen bonding, typical of the polyphenolic compounds abundant in plant extracts. Second, a very strong, very broad band centered at 576 cm^{-1} is observed. While this region is complex, such a low-frequency, broad band is mostly attributed to out-of-plane aromatic ring bending vibrations (γ C–H) or aryl ring deformation modes that are characteristic of complex polyphenolic compounds, such as those found in *K. pinnata* extract.

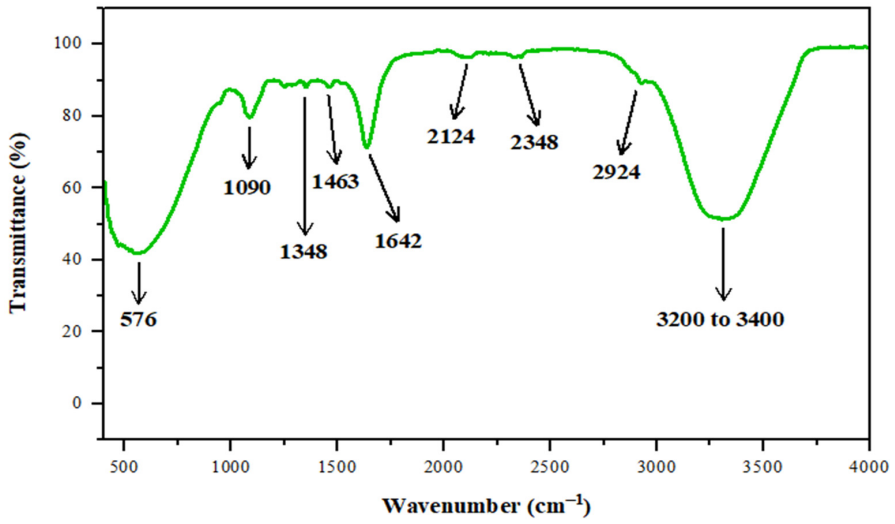


Figure 9. FT-IR spectra of Au NPs.

A medium, sharp peak at 1642 cm^{-1} confirms the presence of carbonyl (C=O) stretching vibrations from ketones, aldehydes, or amide I bands, which are common in phy-

tochemicals. Another medium, sharp peak at 1090 cm^{-1} is assigned to C–O stretching vibrations from alcohols, esters, or ethers.

Several weaker peaks provide additional structural context. The weak, sharp bands at 2924 cm^{-1} (C–H stretch), 2348 cm^{-1} (atmospheric CO_2), 2124 cm^{-1} (C≡N), 1463 cm^{-1}, and 1348 cm^{-1} (C–H/O–H deformations) are present but indicate these functional groups are less dominant in the surface composition.

This confirms that the hydroxyl (–OH) and carbonyl (C=O) functional groups are actively involved in the bioreduction and capping process, with the intense, broad low-frequency band suggesting a strong, coordinated interaction at the nanoparticle surface.

3.3.4. Crystal Structure

The crystallinity and phase purity of the synthesized Au NPs were confirmed using XRD analysis (Figure 10). The diffraction pattern exhibits five distinct, sharp peaks at 2θ values of 38.20°, 44.44°, 64.78°, 77.70°, and 81.76°. These peaks correspond to the crystallographic planes of (111), (200), (220), (311), and (222), respectively [21]. The observed peak positions and their relative intensities are in excellent agreement with the standard diffraction pattern for face-centered cubic crystalline gold (JCPDS card no. 04-0784) [21]. The absence of any other significant diffraction peaks confirms the high purity of the synthesized Au NPs, with no detectable crystalline impurities or oxide phases.

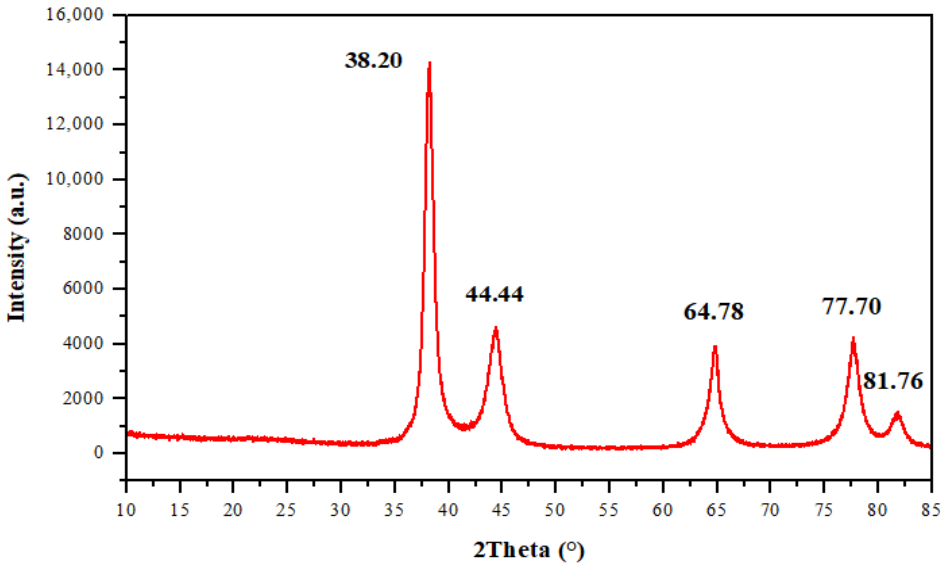


Figure 10. XRD spectra of Au NPs.

The peak broadening observed in the diffractogram is attributed to the nanoscale size of the crystallites. The average crystallite size (D) of the Au NPs was estimated using the Debye–Scherrer formula, $D = K\lambda/(\beta \cos\theta)$, where K is the shape factor (0.9), λ is the X-ray wavelength (Cu Kα = 1.5406 Å), β is the full width at half maximum of the most intense peak (111) in radians, and θ is the Bragg diffraction angle [46]. The calculated average crystallite size was approximately 4.278 nm.

The intense and sharp nature of the (111) peak, compared to other reflections, indicates that this plane is the predominant growth orientation, which is a common characteristic for face-centered cubic metallic NPs synthesized under mild conditions. This XRD analysis conclusively demonstrated the successful formation of phase-pure, crystalline Au NPs via the *K. pinnata* leaf extract-mediated green synthesis process.

3.3.5. BET Analysis

The specific surface area and porosity characteristics of the synthesized Au NPs were investigated using nitrogen adsorption–desorption isotherms analyzed via the BET method (Figure 11).

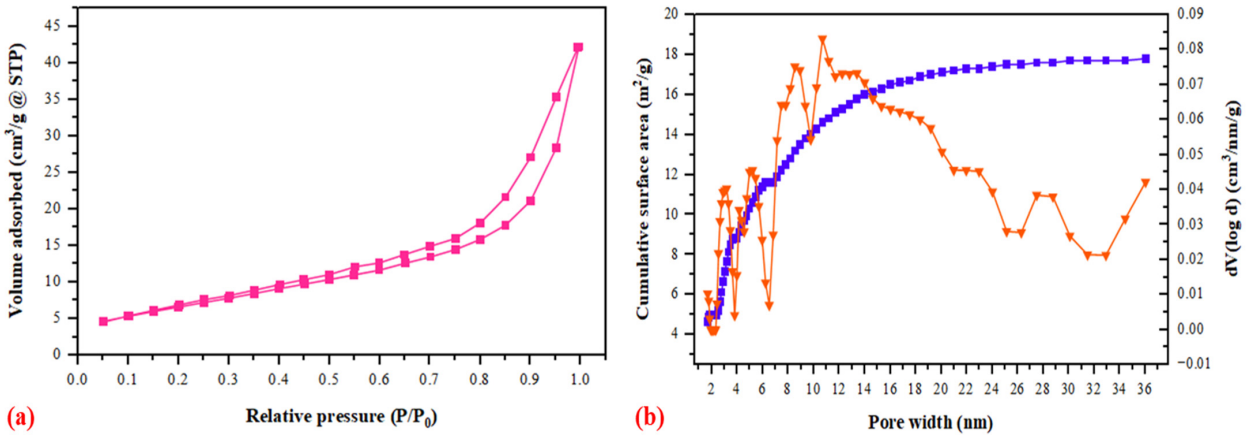


Figure 11. BET analysis of Au NPs. (**a**) Nitrogen adsorption–desorption isotherm and (**b**) pore size distribution curve.

The nitrogen adsorption–desorption isotherm can be classified as Type IV according to the IUPAC classification, which is characteristic of mesoporous materials (pore diameters between 2 and 50 nm) [28]. A distinct H3-type hysteresis loop is observed in the relative pressure (P/P_0) range of approximately 0.4 to 0.9, indicating the presence of slit-shaped pores formed by the aggregation of plate-like NPs. This hysteresis arises from the capillary condensation of nitrogen within the mesoporous structure [47].

The BET specific surface area calculated from the linear region of the isotherm (typically P/P_0 = 0.05 to 0.30) was determined to be 17.46 m^2/g. A high specific surface area is a direct consequence of the nanoscale dimensions of the particles, as confirmed by TEM and DLS analyses.

The total pore volume and average pore diameter were calculated using the Barrett–Joyner–Halenda method applied to the desorption branch of the isotherm. The total pore volume was 0.05 cm^3/g, and the average pore diameter was 16.48 nm, confirming the mesoporous nature of the nanoparticle aggregate network. This porous texture, resulting from interparticle voids, is advantageous for applications requiring high surface accessibility, such as catalysis and sensing, as it facilitates the diffusion of reactants to the active gold surface [48].

3.3.6. Morphology

The TEM analysis (Figure 12) confirms the formation of discrete, well-dispersed Au NPs. The particles predominantly exhibit a spherical morphology, which is consistent with the symmetric SPR band observed in UV-Vis spectroscopy. A histogram generated from measuring over 100 individual particles reveals a size distribution ranging from approximately 19 nm to 34 nm, with an average particle diameter of 26.31 ± 4.1 nm (Figure 12c). This polydispersity is typical for plant-mediated synthesis and is reflected in the moderate polydispersity index value obtained from DLS analysis. TEM images of individual Au NPs (Figure 12b) show clear lattice fringes with an interplanar spacing of ~0.24 nm, corresponding to the (111) plane of face-centered cubic gold. This finding is in excellent agreement with the most intense (111) peak in the XRD pattern, confirming the single-crystalline nature of the Au NPs.

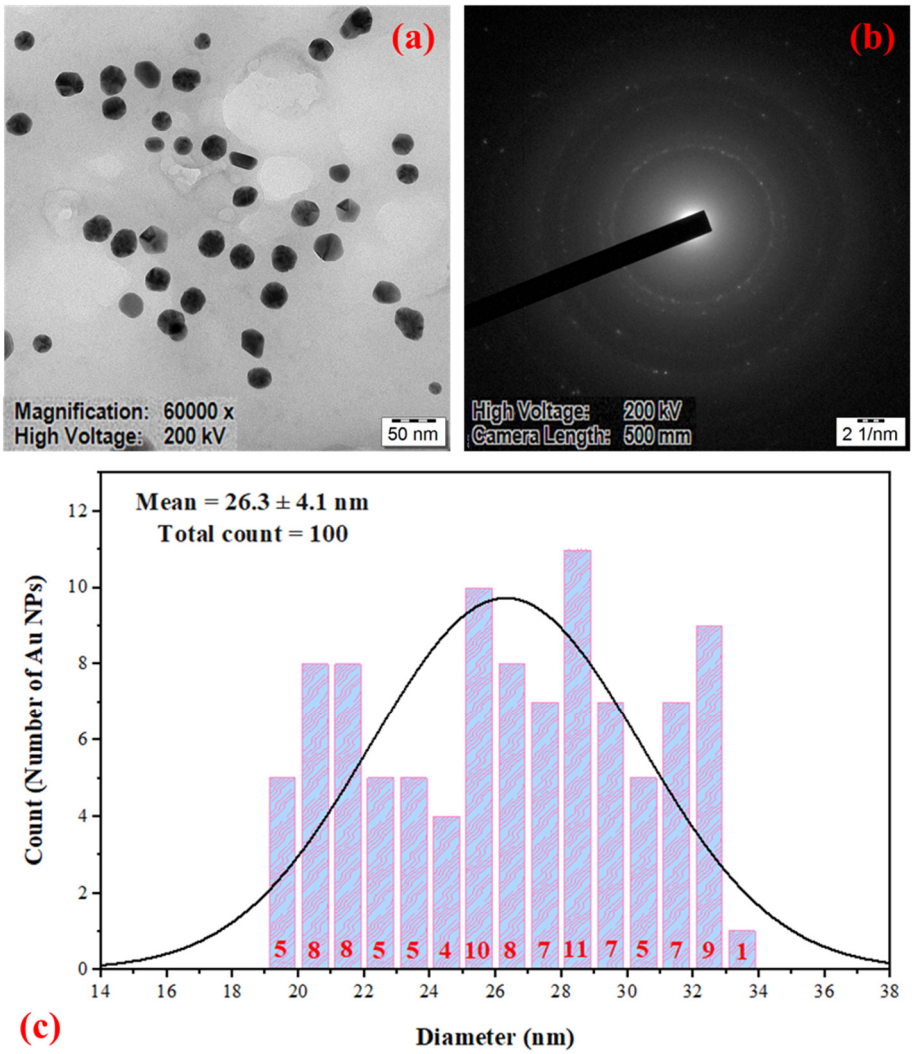


Figure 12. TEM analysis of Au NPs. (**a**) TEM micrograph showing the morphology and dispersion of Au NPs (scale bar: 50 nm). (**b**) High-resolution TEM image showing lattice fringes of fcc Au (scale bar: 2 1/2 nm). (**c**) Particle size distribution histogram with Gaussian fitting using ImageJ software (ImageJ 1.49v, National Institute of Health, Bethesda, MD, USA). The numbers at the bottom of the bars represent the number of Au NPs observed per reported diameter.

3.3.7. Elemental

The EDX spectrum (Figure 13) confirms gold as the primary metallic component, with characteristic Lα and Mα emission peaks corresponding to approximately 5.64 atomic% gold. The spectrum also shows prominent carbon peaks, with an atomic percentage of 94.36%. While these carbon signals originate from the phytochemicals (e.g., polyphenols, flavonoids) of the *K. pinnata* extract associated with the Au NPs, it is important to note that such a high carbon content is unusually elevated for purified metallic NPs. This value likely indicates the presence of a substantial organic matrix associated with the Au NPs, rather than solely representing a surface-bound capping layer. Plant-mediated synthesis often yields NPs with associated biomolecular coronas that may persist even after multiple washing steps. The carbon signal therefore reflects the combined contribution of surface-bound capping agents and potentially residual organic material from the extract. This interpretation is consistent with the FT-IR analysis (Section 3.3.3), which confirms the presence of organic functional groups, and with the negative zeta potential (Section 3.3.2), which suggests surface-associated anionic species. The absence of significant peaks for other elements confirms the absence of inorganic impurities.

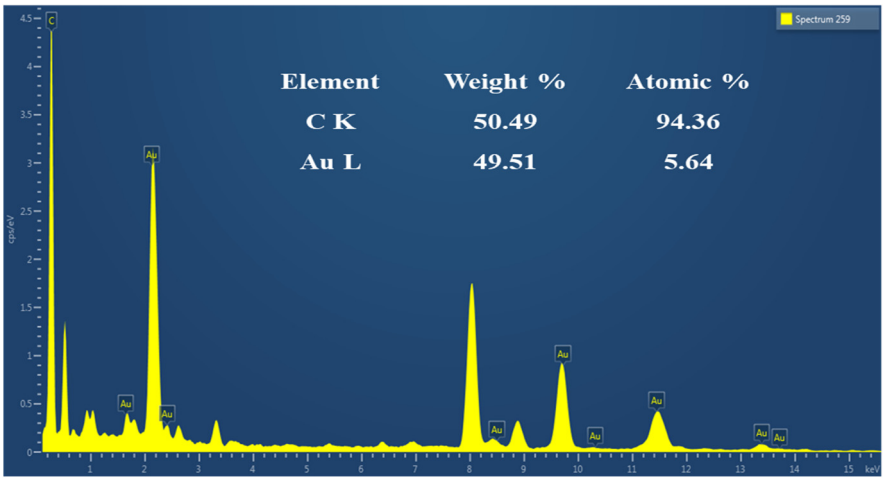


Figure 13. EDX spectra of Au NPs.

3.3.8. Comparative Analysis with the Literature

A comparative analysis of the characterization data (Table S5) situates the properties of the Au NPs synthesized under the optimized conditions clearly within the spectrum of plant-mediated syntheses while highlighting specific advantages. The SPR λ_{max} of 540 nm is consistent with the formation of spherical Au NPs, aligning with values reported for *Ganoderma lucidum* (550 nm) [49] and *Pancratium parvum* (545 nm) [50], and is slightly red-shifted compared to those from *Nothapodytes foetida* (524 nm) [21] or *Ginkgo biloba* (535 nm) [46,51]. This indicated a moderately larger particle size or core-capping assembly, which is confirmed by the TEM average core size of 26.3 nm. The crystallographic structure, confirmed by XRD, shows excellent agreement with the standard face-centered cubic phase of gold. The peak positions (38.20°, 44.44°, 64.78°, 77.70°, 81.76°) match those reported in the literature for pure metallic Au NPs [21,42,44,46,49], and the relative intensity of the (111) plane indicates it as the predominant growth orientation—a common characteristic for face-centered cubic metals synthesized under mild conditions. The crystallite size calculated from the (111) peak broadening (4.28 nm) is smaller than the TEM particle size, suggesting the nanoparticles are polycrystalline, composed of multiple coherently scattering domains. This polycrystallinity is also observed in other biosynthesized Au NPs, such as those from *Passiflora ligularis* (crystallite size 0.14 nm) [21] and *Andrographis paniculata* (25.4 nm) [46]. Crucially, the colloidal stability of our NPs, as indicated by a zeta potential of –30.45 mV, is significantly higher than that reported for *Allium cepa* (–14 mV) [42] and comparable to the excellent stability seen in *N. foetida* (–60.7 mV) [21] *and Lilium wallichianum* (–30.73 mV) [44] synthesized NPs. This strong negative charge, attributed to the anionic phytochemical capping layer from *K. pinnata*, directly supports the observed resistance to aggregation. The substantial organic content (50.49% C from EDX) associated with the particles underscores the effective capping role of the extract, a feature also noted in works with high carbon percentages [42,46,49]. Therefore, while the optical and structural properties are consistent with successful green synthesis, the optimized protocol particularly excels in producing Au NPs with enhanced electrostatic stability and defined crystallinity, a critical combination for long-term storage and application.

4. Conclusions

This study established a statistically validated protocol for the green synthesis of Au NPs using AKPLE. A hybrid experimental strategy, transitioning from OFAT screening to a five-factor BBD, enabled the modeling and simultaneous optimization of two critical optical responses: the SPR peak position (λ_{max}) and its absorbance intensity.

The OFAT experiments identified practical operating ranges for $HAuCl_4$ concentration (0.25 to 2.00 mM), AKPLE concentration (0.5 to 4.0% v/v), reaction temperature (RT to 100 °C), pH (3 to 11), and time (0 to 120 min). Subsequent RSM analysis generated highly predictive quadratic models for both responses ($R^2 > 0.97$), with analysis of variance confirming all main and quadratic effects as statistically significant ($p < 0.0001$). The models revealed that synthesis outcomes are governed primarily by strong nonlinear curvature, with minimal contribution from two-factor interactions within the studied domain.

Multi-response numerical optimization via a desirability function identified a harmonized set of conditions that minimizes λ_{max} while maximizing absorbance. The predicted optimum—$HAuCl_4$ = 0.44 mM, AKPLE = 3.50% v/v, temperature = 80.6 °C, pH = 7.2, and time = 66.7 min—was experimentally validated, yielding Au NPs with an SPR peak at 540 nm and an absorbance of 0.613. Comprehensive characterization confirmed the formation of spherical, crystalline Au NPs with an average TEM core size of 26.3 ± 4.1 nm, excellent colloidal stability (zeta potential = –30.45 mV), and a mesoporous aggregate structure.

In summary, this work demonstrated that an integrated OFAT-RSM approach is superior to conventional single-variable optimization for the green synthesis of Au NPs, as it precisely identifies a multi-factor operating window that balances nanoparticle size and plasmonic absorbance. The statistically robust models provide a validated and scalable framework for optimizing plant-mediated nanomaterial synthesis, contributing to the development of more reproducible and application-specific eco-friendly nanofabrication routes.

Supplementary Materials: The following supporting information can be downloaded at https://www.mdpi.com/article/10.3390/physchem6020022/s1: Table S1: Details of OFAT studies; Table S2: Examples of OFAT studies reported in literature; Table S3: RSM-BBD design table; Table S4: Examples of RSM studies reported in literature; Table S5: Characterization studies of Au NPs synthesized and those reported in literature; Figure S1: (a) Interaction plot showing the combined effect of $HAuCl_4$ concentration (A) and AKPLE concentration (B) on SPR peak position (λ_{max}, nm) at fixed temperature, pH, and time. Predicted λ_{max} is plotted vs $HAuCl_4$ concentration (0.25 to 0.75 mM) at 2 AKPLE levels (B = 2.0 and 3.5% v/v). Other factors were held constant at C (temperature) = 80 °C, D (pH) = 7, and E (time) = 60 min. (b) Interaction plot showing the combined effect of $HAuCl_4$ concentration (A) and temperature (C) on SPR peak position (λ_{max}, nm) at fixed AKPLE concentration, pH, and time. Predicted λ_{max} is plotted vs $HAuCl_4$ concentration (0.25 to 0.75 mM) at 2 temperature levels (C = 70 and 90 °C). Other factors were held constant at B (AKPLE) = 2.75% v/v, D (pH) = 7, and E (time) = 60 min. (c) Interaction plot showing the combined effect of $HAuCl_4$ concentration (A) and pH (D) on SPR peak position (λ_{max}, nm) at fixed AKPLE concentration, temperature, and time. Predicted λ_{max} is plotted vs $HAuCl_4$ concentration (0.25 to 0.75 mM) at 2 pH levels (D = 5 and 9). Other factors were held constant at B (AKPLE) = 2.75% v/v, C (temperature) = 80 °C, and E (time) = 60 min. (d) Interaction plot showing the combined effect of $HAuCl_4$ concentration (A) and reaction time (E) on SPR peak position (λ_{max}, nm) at fixed AKPLE concentration, temperature, and pH. Predicted λ_{max} is plotted vs $HAuCl_4$ concentration (0.25 to 0.75 mM) at 2 reaction times (E = 30 and 90 min). Other factors were held constant at B (AKPLE) = 2.75% v/v, C (temperature) = 80 °C, and D (pH) = 7; Figure S2: (a) Interaction plot showing the combined effect of AKPLE concentration (B) and temperature (C) on SPR peak position (λ_{max}, nm) at fixed $HAuCl_4$ concentration, pH, and time. Predicted λ_{max} is plotted vs AKPLE concentration (2.0 to 3.5% v/v) at 2 temperature levels (C = 70 and 90 °C). Other factors were held constant at A ($HAuCl_4$) = 0.50 mM, D (pH) = 7, and E (time) = 60 min. (b) Interaction plot showing the combined effect of AKPLE concentration (B) and pH (D) on SPR peak position (λ_{max}, nm) at fixed $HAuCl_4$ concentration, temperature, and time. Predicted λ_{max} is plotted vs AKPLE concentration (2.0 to 3.5% v/v) at 2 pH levels (D = 5 and 9). Other factors were held constant at A ($HAuCl_4$) = 0.50 mM, C (temperature) = 80 °C, and E (time) = 60 min. (c) Interaction plot showing the combined effect of AKPLE concentration (B) and reaction time (E) on SPR peak position (λ_{max}, nm) at fixed $HAuCl_4$ concentration, temperature, and pH. Predicted λ_{max} is plotted vs AKPLE concentration (2.0 to 3.5% v/v) at 2 reaction times (E = 30 and 90 min).

Other factors were held constant at A ($HAuCl_4$) = 0.50 mM, C (temperature) = 80 °C, and D (pH) = 7; Figure S3: (a) Interaction plot showing the combined effect of temperature (C) and pH (D) on SPR peak position (λ_{max}, nm) at fixed $HAuCl_4$ concentration, AKPLE concentration, and time. Predicted λ_{max} is plotted vs temperature (70 to 90 °C) at 2 pH levels (D = 5 and 9). Other factors were held constant at A ($HAuCl_4$) = 0.50 mM, B (AKPLE) = 2.75% v/v, and E (time) = 60 min. (b) Interaction plot showing the combined effect of temperature (C) and reaction time (E) on SPR peak position (λ_{max}, nm) at fixed $HAuCl_4$ concentration, AKPLE concentration, and pH. Predicted λ_{max} is plotted vs temperature (70 to 90 °C) at 2 reaction times (E = 30 and 90 min). Other factors were held constant at A ($HAuCl_4$) = 0.50 mM, B (AKPLE) = 2.75% v/v, and D (pH) = 7. (c) Interaction plot showing the combined effect of pH (D) and reaction time (E) on SPR peak position (λ_{max}, nm) at fixed $HAuCl_4$ concentration, AKPLE concentration, and temperature. Predicted λ_{max} is plotted vs pH (5 to 9) at 2 reaction times (E = 30 and 90 min). Other factors were held constant at A ($HAuCl_4$) = 0.50 mM, B (AKPLE) = 2.75% v/v, and C (temperature) = 80 °C; Figure S4: (a) Interaction plot showing the combined effect of $HAuCl_4$ concentration (A) and AKPLE concentration (B) on absorbance at the SPR maximum (absorbance at λ_{max}, a.u.) at fixed temperature, pH, and time. Predicted absorbance at λ_{max} is plotted vs $HAuCl_4$ concentration (0.25 to 0.75 mM) at 2 AKPLE levels (B = 2.0 and 3.5% v/v). Other factors were held constant at C (temperature) = 80 °C, D (pH) = 7, and E (time) = 60 min. (b) Interaction plot showing the combined effect of $HAuCl_4$ concentration (A) and temperature (C) on absorbance at the SPR maximum (absorbance at λ_{max}) at fixed AKPLE concentration, pH, and time. Predicted absorbance at λ_{max} is plotted vs $HAuCl_4$ concentration (0.25 to 0.75 mM) at 2 temperature levels (C = 70 and 90 °C). Other factors were held constant at B (AKPLE) = 2.75% v/v, D (pH) = 7, and E (time) = 60 min. (c) Interaction plot showing the combined effect of $HAuCl_4$ concentration (A) and pH (D) on absorbance at the SPR maximum (absorbance at λ_{max}) at fixed AKPLE concentration, temperature, and time. Predicted absorbance at λ_{max} is plotted vs $HAuCl_4$ concentration (0.25 to 0.75 mM) at 2 pH levels (D = 5 and 9). Other factors were held constant at B (AKPLE) = 2.75% v/v, C (temperature) = 80 °C, and E (time) = 60 min. (d) Interaction plot showing the combined effect of $HAuCl_4$ concentration (A) and reaction time (E) on absorbance at the SPR maximum (absorbance at λ_{max}) at fixed AKPLE concentration, temperature, and pH. Predicted absorbance at λ_{max} is plotted vs $HAuCl_4$ concentration (0.25 to 0.75 mM) at 2 reaction times (E = 30 and 90 min). Other factors were held constant at B (AKPLE) = 2.75% v/v, C (temperature) = 80 °C, and D (pH) = 7; Figure S5: (a) Interaction plot showing the combined effect of AKPLE concentration (B) and temperature (C) on absorbance at the SPR maximum (absorbance at λ_{max}) at fixed $HAuCl_4$ concentration, pH, and time. Predicted absorbance at λ_{max} is plotted vs AKPLE concentration (2.0 to 3.5% v/v) at 2 temperature levels (C = 70 and 90 °C). Other factors were held constant at A ($HAuCl_4$) = 0.50 mM, D (pH) = 7, and E (time) = 60 min. (b) Interaction plot showing the combined effect of AKPLE concentration (B) and pH (D) on absorbance at the SPR maximum (absorbance at λ_{max}) at fixed $HAuCl_4$ concentration, temperature, and time. Predicted absorbance at λ_{max} is plotted vs AKPLE concentration (2.0 to 3.5% v/v) at 2 pH levels (D = 5 and 9). Other factors were held constant at A ($HAuCl_4$) = 0.50 mM, C (temperature) = 80 °C, and E (time) = 60 min. (c) Interaction plot showing the combined effect of AKPLE concentration (B) and reaction time (E) on absorbance at the SPR maximum (absorbance at λ_{max}) at fixed $HAuCl_4$ concentration, temperature, and pH. Predicted absorbance at λ_{max} is plotted vs AKPLE concentration (2.0 to 3.5% v/v) at 2 reaction times (E = 30 and 90 min). Other factors were held constant at A ($HAuCl_4$) = 0.50 mM, C (temperature) = 80 °C, and D (pH) = 7; Figure S6: (a) Interaction plot showing the combined effect of temperature (C) and pH (D) on absorbance at the SPR maximum (absorbance at λ_{max}) at fixed $HAuCl_4$ concentration, AKPLE concentration, and time. Predicted absorbance at λ_{max} is plotted vs temperature (70 to 90 °C) at 2 pH levels (D = 5 and 9). Other factors were held constant at A ($HAuCl_4$) = 0.50 mM, B (AKPLE) = 2.75% v/v, and E (time) = 60 min. (b) Interaction plot showing the combined effect of temperature (C) and reaction time (E) on absorbance at the SPR maximum (absorbance at λ_{max}) at fixed $HAuCl_4$ concentration, AKPLE concentration, and pH. Predicted absorbance at λ_{max} is plotted vs temperature (70 to 90 °C) at 2 reaction times (E = 30 and 90 min). Other factors were held constant at A ($HAuCl_4$) = 0.50 mM, B (AKPLE) = 2.75% v/v, and D (pH) = 7. (c) Interaction plot showing the

combined effect of pH (D) and reaction time (E) on absorbance at the SPR maximum (absorbance at λ_{max}) at fixed $HAuCl_4$ concentration, AKPLE concentration, and temperature. Predicted absorbance at λ_{max} is plotted vs pH (5 to 9) at 2 reaction times (E = 30 and 90 min). Other factors were held constant at A ($HAuCl_4$) = 0.50 mM, B (AKPLE) = 2.75% v/v, and C (temperature) = 80 °C; Figure S7: (a) Response surface for the combined effect of $HAuCl_4$ concentration and AKPLE concentration on SPR peak position (λ_{max}, nm). 3D response surface with corresponding contour projection showing the quadratic-model-predicted SPR peak position (λ_{max}, nm) as a function of $HAuCl_4$ concentration (A; 0.25 to 0.75 mM) and AKPLE concentration (B; 2.0 to 3.5% v/v), with temperature (C) fixed at 78 °C, pH (D) fixed at 7, and reaction time (E) fixed at 60 min; the color scale represents predicted λ_{max} across the design space. (b) Response surface for the combined effect of $HAuCl_4$ concentration and AKPLE concentration on absorbance at the SPR maximum (absorbance at λ_{max}). 3D response surface with contour projection showing the quadratic-model-predicted absorbance at λ_{max} as a function of $HAuCl_4$ concentration (A; 0.25 to 0.75 mM) and AKPLE concentration (B; 2.0 to 3.5% v/v), with temperature (C) fixed at 80 °C, pH (D) fixed at 7, and reaction time (E) fixed at 60 min; experimental design points are overlaid to visualize agreement with model predictions; Figure S8: (a) Response surface for the combined effect of $HAuCl_4$ concentration and temperature on SPR peak position (λ_{max}, nm). 3D response surface with contour projection showing the quadratic-model-predicted SPR peak position (λmax, nm) as a function of $HAuCl_4$ concentration (A; 0.25 to 0.75 mM) and temperature (C; 70 to 90 °C), with AKPLE concentration (B) fixed at 2.75% (v/v), pH (D) fixed at 7, and reaction time (E) fixed at 60 min; overlaid symbols denote experimental design points relative to model predictions. (b) Response surface for the combined effect of $HAuCl_4$ concentration and temperature on absorbance at the SPR maximum (absorbance at λ_{max}). 3D response surface with contour projection showing the quadratic-model-predicted absorbance at λ_{max} as a function of $HAuCl_4$ concentration (A; 0.25 to 0.75 mM) and temperature (C; 70 to 90 °C), with AKPLE concentration (B) fixed at 2.75% (v/v), pH (D) fixed at 7, and reaction time (E) fixed at 60 min; experimental design points are overlaid to visualize agreement with model predictions; Figure S9: (a) Response surface for the combined effect of $HAuCl_4$ concentration and pH on SPR peak position (λ_{max}, nm). 3D response surface with contour projection showing the quadratic-model-predicted SPR peak position (λ_{max}, nm) as a function of $HAuCl_4$ concentration (A; 0.25 to 0.75 mM) and pH (D; 5 to 9), with AKPLE concentration (B) fixed at 2.75% (v/v), temperature (D) fixed at 78 °C, and reaction time (E) fixed at 60 min; the color scale represents predicted λ_{max} across the A to D domain. (b) Response surface for the combined effect of $HAuCl_4$ concentration and pH on absorbance at the SPR maximum (absorbance at λ_{max}). 3D response surface with contour projection showing the quadratic-model-predicted absorbance at λ_{max} as a function of $HAuCl_4$ concentration (A; 0.25 to 0.75 mM) and pH (D; 5 to 9), with AKPLE concentration (B) fixed at 2.75% (v/v), temperature (D) fixed at 80 °C, and reaction time (E) fixed at 60 min; experimental design points are overlaid to visualize agreement with model predictions; Figure S10: (a) Response surface for the combined effect of $HAuCl_4$ concentration and reaction time on SPR peak position (λ_{max}, nm). 3D response surface with contour projection showing the quadratic-model-predicted SPR peak position (λ_{max}, nm) as a function of $HAuCl_4$ concentration (A; 0.25 to 0.75 mM) and reaction time (E; 30 to 90 min), with AKPLE concentration (B) fixed at 2.75% (v/v), temperature (C) fixed at 78 °C, and pH (D) fixed at 7; the color scale represents predicted λ_{max} across the A to E domain. (b) Response surface for the combined effect of $HAuCl_4$ concentration and reaction time on absorbance at the SPR maximum (absorbance at λ_{max}). 3D response surface with contour projection showing the quadratic-model-predicted absorbance at λ_{max} as a function of $HAuCl_4$ concentration (A; 0.25 to 0.75 mM) and reaction time (E; 30 to 90 min), with AKPLE concentration (B) fixed at 2.75% (v/v), temperature (C) fixed at 80 °C, and pH (D) fixed at 7; experimental design points are overlaid to visualize agreement with model predictions; Figure S11: (a) Response surface for the combined effect of AKPLE concentration and temperature on SPR peak position (λ_{max}, nm). 3D response surface with contour projection showing the quadratic-model-predicted SPR peak position (λ_{max}, nm) as a function of AKPLE concentration (B; 2.0 to 3.5% v/v) and temperature (C; 70 to 90 °C), with $HAuCl_4$ concentration (A) fixed at 0.50 mM, pH (D) fixed at 7, and reaction time (E) fixed at 60 min; overlaid symbols denote experimental design points relative to model predictions. (b) Response

surface for the combined effect of AKPLE concentration and temperature on absorbance at the SPR maximum (absorbance at λ_{max}). 3D response surface with contour projection showing the quadratic-model-predicted absorbance at λ_{max} as a function of AKPLE concentration (B; 2.0 to 3.5% v/v) and temperature (C; 70 to 90 °C), with $HAuCl_4$ concentration (A) fixed at 0.50 mM, pH (D) fixed at 7, and reaction time (E) fixed at 60 min; experimental design points are overlaid to visualize agreement with model predictions; Figure S12: (a) Response surface for the combined effect of AKPLE concentration and pH on SPR peak position (λ_{max}, nm). 3D response surface with contour projection showing the quadratic-model-predicted SPR peak position (λ_{max}, nm) as a function of AKPLE concentration (B; 2.0 to 3.5% v/v) and pH (D; 5 to 9), with $HAuCl_4$ concentration (A) fixed at 0.50 mM, temperature (C) fixed at 78 °C, and reaction time (E) fixed at 60 min; the color scale represents predicted λ_{max} across the B to D domain. (b) Response surface for the combined effect of AKPLE concentration and pH on absorbance at the SPR maximum (absorbance at λ_{max}). 3D response surface with contour projection showing the quadratic-model-predicted absorbance at λ_{max} as a function of AKPLE concentration (B; 2.0 to 3.5% v/v) and pH (D; 5 to 9), with $HAuCl_4$ concentration (A) fixed at 0.50 mM, temperature (D) fixed at 80 °C, and reaction time (E) fixed at 60 min; experimental design points are overlaid to visualize agreement with model predictions; Figure S13: (a) Response surface for the combined effect of AKPLE concentration and reaction time on SPR peak position (λ_{max}, nm). 3D response surface with contour projection showing the quadratic-model-predicted SPR peak position (λ_{max}, nm) as a function of AKPLE concentration (B; 2.0 to 3.5% v/v) and reaction time (E; 30 to 90 min), with $HAuCl_4$ concentration (A) fixed at 0.50 mM, temperature (C) fixed at 78 °C, and pH (D) fixed at 7; the color scale represents predicted λ_{max} across the B to E domain. (b) Response surface for the combined effect of AKPLE concentration and reaction time on absorbance at the SPR maximum (absorbance at λ_{max}). 3D response surface with contour projection showing the quadratic-model-predicted absorbance at λ_{max} as a function of AKPLE concentration (B; 2.0 to 3.5% v/v) and reaction time (E; 30 to 90 min), with $HAuCl_4$ concentration (A) fixed at 0.50 mM, temperature (C) fixed at 80 °C, and pH (D) fixed at 7; experimental design points are overlaid to visualize agreement with model predictions; Figure S14: (a) Response surface for the combined effect of temperature and pH on SPR peak position (λ_{max}, nm). 3D response surface with contour projection showing the quadratic-model-predicted SPR peak position (λ_{max}, nm) as a function of temperature (C; 70 to 90 °C) and pH (D; 5 to 9), with $HAuCl_4$ concentration (A) fixed at 0.50 mM, AKPLE concentration (B) fixed at 2.75% (v/v), and reaction time (E) fixed at 60 min; overlaid symbols denote experimental design points relative to model predictions. (b) Response surface for the combined effect of temperature and pH on absorbance at the SPR maximum (absorbance at λ_{max}). 3D response surface with contour projection showing the quadratic-model-predicted absorbance at λ_{max} as a function of temperature (C; 70 to 90 °C) and pH (D; 5 to 9), with $HAuCl_4$ concentration (A) fixed at 0.50 mM, AKPLE concentration (B) fixed at 2.75% (v/v), and reaction time (E) fixed at 60 min; experimental design points are overlaid to visualize agreement with model predictions; Figure S15: (a) Response surface for the combined effect of temperature and reaction time on SPR peak position (λ_{max}, nm). 3D response surface with contour projection showing the quadratic-model-predicted SPR peak position (λ_{max}, nm) as a function of temperature (C; 70 to 90 °C) and reaction time (E; 30 to 90 min), with $HAuCl_4$ concentration (A) fixed at 0.50 mM, AKPLE concentration (B) fixed at 2.75% (v/v), and pH (D) fixed at 7; overlaid symbols denote experimental design points relative to model predictions. (b) Response surface for the combined effect of temperature and reaction time on absorbance at the SPR maximum (absorbance at λ_{max}). 3D response surface with contour projection showing the quadratic-model-predicted absorbance at λ_{max} as a function of temperature (C; 70 to 90 °C) and reaction time (E; 30 to 90 min), with $HAuCl_4$ concentration (A) fixed at 0.50 mM, AKPLE concentration (B) fixed at 2.75% (v/v), and pH (D) fixed at 7; experimental design points are overlaid to visualize agreement with model predictions; Figure S16: (a) Response surface for the combined effect of reaction pH and reaction time on on SPR peak position (λ_{max}, nm). 3D response surface with contour projection showing the quadratic-model-predicted SPR peak position (λ_{max}, nm) as a function of reaction pH (D; 5 to 9) and reaction time (E; 30 to 90 min), with $HAuCl_4$ concentration (A) fixed at 0.50 mM, AKPLE concentration (B) fixed at 2.75% (v/v), and temperature (C) fixed at 78 °C; overlaid symbols denote experimental design points relative to model

predictions. (b) Response surface for the combined effect of pH and reaction time on absorbance at the SPR maximum (absorbance at λ_{max}). 3D response surface with contour projection showing the quadratic-model-predicted absorbance at λ_{max} as a function of pH (D; 5 to 9) and reaction time (E; 30 to 90 min), with $HAuCl_4$ concentration (A) fixed at 0.50 mM, AKPLE concentration (B) fixed at 2.75% (v/v), and temperature (C) fixed at 80 °C; experimental design points are overlaid to visualize agreement with model predictions; Figure S17: Numerical optimization (desirability function) for simultaneous minimization of SPR peak position (λ_{max}, nm) and maximization of absorbance at λ_{max} under the RSM-BBD model. Factor bounds were constrained to the experimental ranges: A ($HAuCl_4$, 0.25 to 0.75 mM), B (AKPLE, 2.0 to 3.5% v/v), C (temperature, 70 to 90 °C), D (pH, 5 to 9), and E (time, 30 to 90 min). Goals were set to minimize λ_{max} and maximize absorbance at λ_{max}. The software returns the best-ranked solution (solution 1 of 100) with overall desirability equal to 1.000.

Author Contributions: S.M.: Conceptualization, methodology, investigation, data curation, formal analysis, and writing—original draft. H.K.: Methodology, data curation, formal analysis, and writing—original draft. A.V.: Formal analysis, visualization, software, writing—original draft, and writing—review and editing. P.K.G.: Software, visualization, and writing—review and editing. S.D.: Visualization, writing—original draft, and writing—review and editing. V.G.: Conceptualization, formal analysis, writing—review and editing, resources, project administration, and supervision. All authors have read and agreed to the published version of the manuscript.

Funding: This research received no external funding.

Data Availability Statement: The original contributions presented in this study are included in the article/Supplementary Material. Further inquiries can be directed to the corresponding author.

Acknowledgments: The authors thank Principal and Management, Vaagdevi Degree and P.G. College, Warangal (Telangana, India), for providing the required laboratory facilities for this work. During the preparation of this work, the authors used Grammarly in order to improve the readability and sentence structure. After using this tool/service, the authors reviewed and edited the content as needed and take full responsibility for the content of the publication.

Conflicts of Interest: The authors declare no conflicts of interest.

Abbreviations

The following abbreviations are used in this manuscript:

AKPLE	Aqueous *Kalanchoe pinnata* leaf extract
ANOVA	Analysis of variance
Au NPs	Gold nanoparticles
BBD	Box–Behnken Design
BET	Brunauer–Emmett–Teller
DLS	Dynamic light scattering
EDX	Energy-dispersive X-ray spectroscopy
FT-IR	Fourier transform infrared
OFAT	One-factor-at-a-time
RSM	Response surface methodology
SPR	Surface plasmon resonance
TEM	Transmission electron microscopy
UV-Vis	Ultraviolet–visible
XRD	X-ray diffraction

References

1. Gul, M.; Kashif, M.; Muhammad, S.; Azizi, S.; Sun, H. Various Methods of Synthesis and Applications of Gold-Based Nanomaterials: A Detailed Review. *Cryst. Growth Des.* **2025**, *25*, 2227–2266. [CrossRef]
2. Sati, A.; Mali, S.N.; Samdani, N.; Annadurai, S.; Dongre, R.; Satpute, N.; Ranade, T.N.; Pratap, A.P. From Past to Present: Gold Nanoparticles (AuNPs) in Daily Life–Synthesis Mechanisms, Influencing Factors, Characterization, Toxicity, and Emerging Applications in Biomedicine, Nanoelectronics, and Materials Science. *ACS Omega* **2025**, *10*, 33999–34087. [CrossRef] [PubMed]
3. Shah, S.S.; Zentou, H.; Shaikh, M.N.; Hussain, A.; Helal, A.; Islam, N.; Uddin, S.; Ogawa, T.; Aziz, M.A. Ultra-Simple and Cost-Effective Synthesis of Highly Stable, Biocompatible, Carboxylic-Functionalized Gold Nanoparticles by Pamoic Acid for Advanced Applications. *Chem. Rec.* **2025**, *26*, e202500213. [CrossRef] [PubMed]
4. Dinh, T.; Dobó, Z.; Palotás, Á.B.; Kovács, H. A Review of Gold Nanoparticle Synthesis: Transitioning from Conventional Techniques to Plant-Mediated Green Nanofabrication. *Mater. Today Chem.* **2025**, *48*, 103003. [CrossRef]
5. Mehdi, J.; Ansari, V.A.; Singh, A. A Review of Gold Nanoparticles: Synthesis Methods and Biomedical Applications. *Biomed. Mater. Devices* **2025**, *26*, 1–17. [CrossRef]
6. Mehra, V.; Kumar, S.; Tamang, A.M.; Chandraker, S.K. Green Synthesis of Gold Nanoparticles (AuNPs) by Using Plant Extract and Their Biological Application: A Review. *Bionanoscience* **2025**, *15*, 18. [CrossRef]
7. Huq, M.A.; Rana, M.R.; Samad, A.; Rahman, M.S.; Rahman, M.M.; Ashrafudoulla, M.; Akter, S.; Park, J.-W. Green Synthesis, Characterization, and Potential Antibacterial and Anticancer Applications of Gold Nanoparticles: Current Status and Future Prospects. *Biomedicines* **2025**, *13*, 1184. [CrossRef]
8. Pattanashetti, L.; Donagannavar, M.M.; Jigalur, D.; Patil, V.S. *Bryophyllum pinnatum* (L.) Pers. Modulates Multiple Neuroprotective Targets in Alzheimer's Disease: Evidence from Computational and Experimental Validation. *Cell Biochem. Biophys.* **2025**, *83*, 5141–5166. [CrossRef]
9. Nascimento, L.B.D.S.; Casanova, L.M.; Costa, S.S. Bioactive Compounds from *Kalanchoe* Genus Potentially Useful for the Development of New Drugs. *Life* **2023**, *13*, 646. [CrossRef]
10. Sharma, G.; Jangra, A.; Sihag, S.; Chaturvedi, S.; Yadav, S.; Chhokar, V. *Bryophyllum pinnatum* (Lam.) Oken: Unravelling Therapeutic Potential and Navigating Toxicity. *Physiol. Mol. Biol. Plants* **2024**, *30*, 1413–1427. [CrossRef] [PubMed]
11. Al-Radadi, N.S. *Ephedra* Mediated Green Synthesis of Gold Nanoparticles (AuNPs) and Evaluation of Its Antioxidant, Antipyretic, Anti-Asthmatic, and Antimicrobial Properties. *Arab. J. Chem.* **2023**, *16*, 104353. [CrossRef]
12. Do Dat, T.; Cong, C.Q.; Le Hoai Nhi, T.; Khang, P.T.; Nam, N.T.H.; Thi Tinh, N.; Hue, D.T.; Hieu, N.H. Green Synthesis of Gold Nanoparticles Using *Andrographis paniculata* Leave Extract for Lead Ion Detection, Degradation of Dyes, and Bioactivities. *Biochem. Eng. J.* **2023**, *200*, 109103. [CrossRef]
13. Nayak, S.; Sajankila, S.P.; Goveas, L.C.; Rao, V.C.; Mutalik, S.; Shreya, B.A. Two Fold Increase in Synthesis of Gold Nanoparticles Assisted by Proteins and Phenolic Compounds in *Pongamia* Seed Cake Extract: Response Surface Methodology Approach. *SN Appl. Sci.* **2020**, *2*, 634. [CrossRef]
14. Al-Radadi, N.S.; Al-Bishri, W.M.; Salem, N.A.; ElShebiney, S.A. Plant-Mediated Green Synthesis of Gold Nanoparticles Using an Aqueous Extract of *Passiflora ligularis*, Optimization, Characterizations, and Their Neuroprotective Effect on Propionic Acid-Induced Autism in Wistar Rats. *Saudi Pharm. J.* **2024**, *32*, 101921. [CrossRef]
15. Ghoreishi, S.M.; Mortazavi-Derazkola, S. Eco-Friendly Synthesis of Gold Nanoparticles via Tangerine Peel Extract: Unveiling Their Multifaceted Biological and Catalytic Potentials. *Heliyon* **2025**, *11*, e40104. [CrossRef] [PubMed]
16. Nguyen, T.H.A.; Nguyen, V.-C.; Phan, T.N.H.; Le, V.T.; Vasseghian, Y.; Trubitsyn, M.A.; Nguyen, A.-T.; Chau, T.P.; Doan, V.-D. Novel Biogenic Silver and Gold Nanoparticles for Multifunctional Applications: Green Synthesis, Catalytic and Antibacterial Activity, and Colorimetric Detection of Fe(III) Ions. *Chemosphere* **2022**, *287*, 132271. [CrossRef] [PubMed]
17. Zannotti, M.; Piras, S.; Remia, L.; Appignanesi, D.; Giovannetti, R. Selective Colorimetric Detection of Pb(II) Ions by Using Green Synthesized Gold Nanoparticles with Orange Peel Extract. *Chemosensors* **2024**, *12*, 33. [CrossRef]
18. Aji, A.; Oktafiani, D.; Yuniarto, A.; Amin, A.K. Biosynthesis of Gold Nanoparticles Using Kapok (*Ceiba pentandra*) Leaf Aqueous Extract and Investigating Their Antioxidant Activity. *J. Mol. Struct.* **2022**, *1270*, 133906. [CrossRef]
19. Patil, D.N.; Patil, P.J.; Rane, M.R.; Yadav, S.R.; Bapat, V.A.; Vyavahare, G.D.; Jadhav, J.P. Response Surface Methodology-Based Optimization of *Pancratium parvum* Dalzell-Mediated Synthesis of Gold Nanoparticles with Potential Biomedical Applications. *Int. Nano Lett.* **2021**, *11*, 215–232. [CrossRef]
20. Queen, J.E.; Prasad, T.A.A.; Vithiya, B.S.M.; Odhah, O.H.; Kumar, N.S.; Tamizhdurai, P.; Alreshaidan, S.B.; Basivi, P.K.; Pabba, D.P.; Al-Fatesh, A.S. Optimized Green Synthesis of Gold Nanoparticles from Cranberry Fruit Extract Using Response Surface Methodology for Enhanced Biomedical Applications and Catalytic Degradation. *Bioorg. Chem.* **2025**, *161*, 108546. [CrossRef]
21. Susanna, D.; Balakrishnan, R.M.; Ponnan Ettiyappan, J. Ultrasonication-Assisted Green Synthesis and Characterization of Gold Nanoparticles from *Nothapodytes foetida*: An Assessment of Their Antioxidant, Antibacterial, Anticancer and Wound Healing Potential. *J. Drug Deliv. Sci. Technol.* **2023**, *87*, 104740. [CrossRef]

22. Yu, T.; Liu, L.; Liu, Y.; Yin, W. Synthesis of Gold Nanoparticles Using *Ginkgo biloba* Leaf Extract and Its in Vitro Anticancer Effects on Nasopharyngeal Carcinoma Cells. *Alex. Eng. J.* **2024**, *104*, 614–620. [CrossRef]
23. Rajeshkumar, S.; Sherif, M.H.; Malarkodi, C.; Ponnanikajamideen, M.; Arasu, M.V.; Al-Dhabi, N.A.; Roopan, S.M. Cytotoxicity Behaviour of Response Surface Model Optimized Gold Nanoparticles by Utilizing Fucoidan Extracted from *Padina tetrastromatica*. *J. Mol. Struct.* **2021**, *1228*, 129440. [CrossRef]
24. Kurra, H.; Velidandi, A.; Sarvepalli, M.; Pabbathi, N.P.P.; Godishala, V. Aqueous *Cymbopogon citratus* Extract Mediated Silver Nanoparticles: Part I. Influence of Synthesis Parameters, Characterization, and Biomedical Studies. *Nanomaterials* **2025**, *15*, 328. [CrossRef] [PubMed]
25. Velidandi, A.; Sarvepalli, M.; Aramanda, P.; Amudala, M.L.; Baadhe, R.R. Effect of Size on Physicochemical, Antibacterial, and Catalytic Properties of *Neolamarckia cadamba* (Burflower-Tree) Synthesized Silver/Silver Chloride Nanoparticles. *Environ. Sci. Pollut. Res.* **2023**, *30*, 63231–63249. [CrossRef]
26. Velidandi, A.; Pabbathi, N.P.P.; Dahariya, S.; Kagithoju, S.; Baadhe, R.R. Bio-Fabrication of Silver-Silver Chloride Nanoparticles Using *Annona muricata* Leaf Extract: Characterization, Biological, Dye Degradation and Eco-Toxicity Studies. *Int. J. Environ. Sci. Technol.* **2022**, *19*, 6555–6572. [CrossRef]
27. Velidandi, A.; Sarvepalli, M.; Gandam, P.K.; Prashanth Pabbathi, N.P.; Baadhe, R.R. Characterization, Catalytic, and Recyclability Studies of Nano-Sized Spherical Palladium Particles Synthesized Using Aqueous Poly-Extract (Turmeric, Neem, and Tulasi). *Environ. Res.* **2023**, *228*, 115821. [CrossRef]
28. Sivagami, M.; Asharani, I.V. Catalytic Reduction of Nitroarenes by *Cucumis maderaspatanus* L. Leaves Extract Mediated Silver Nanoparticles. *J. Taiwan Inst. Chem. Eng.* **2023**, *149*, 104981. [CrossRef]
29. Singaravelu, S.; Motsoene, F.; Abrahamse, H.; Dhilip Kumar, S.S. Green-Synthesized Metal Nanoparticles: A Promising Approach for Accelerated Wound Healing. *Front. Bioeng. Biotechnol.* **2025**, *13*, 1637589. [CrossRef] [PubMed]
30. Deka, K.; Nongbet, R.D.; Das, K.; Saikia, P.; Kaur, S.; Talukder, A.; Thakuria, B. Understanding the Mechanism Underlying the Green Synthesis of Metallic Nanoparticles Using Plant Extract(s) with Special Reference to Silver, Gold, Copper and Zinc Oxide Nanoparticles. *Hybrid Adv.* **2025**, *9*, 100399. [CrossRef]
31. Rabiee, N. Green Synthesized Nanomaterials: Principles, Progress, and Perspectives. In *ACS Symposium Series*; ACS Publications: Washington, DC, USA, 2025; pp. 1–27.
32. Vinukonda, A.; Bolledla, N.; Jadi, R.K.; Chinthala, R.; Devadasu, V.R. Synthesis of Nanoparticles Using Advanced Techniques. *Next Nanotechnol.* **2025**, *8*, 100169. [CrossRef]
33. He, M.; Ai, Y.; Hu, W.; Guan, L.; Ding, M.; Liang, Q. Recent Advances of Seed-Mediated Growth of Metal Nanoparticles: From Growth to Applications. *Adv. Mater.* **2023**, *35*, 2211915. [CrossRef]
34. Kaningini, A.G.; Azizi, S.; Sintwa, N.; Mokalane, K.; Mohale, K.C.; Mudau, F.N.; Maaza, M. Effect of Optimized Precursor Concentration, Temperature, and Doping on Optical Properties of ZnO Nanoparticles Synthesized via a Green Route Using Bush Tea (*Athrixia phylicoides* DC.) Leaf Extracts. *ACS Omega* **2022**, *7*, 31658–31666. [CrossRef]
35. Singh, H.; Desimone, M.F.; Pandya, S.; Jasani, S.; George, N.; Adnan, M.; Aldarhami, A.; Bazaid, A.S.; Alderhami, S.A. Revisiting the Green Synthesis of Nanoparticles: Uncovering Influences of Plant Extracts as Reducing Agents for Enhanced Synthesis Efficiency and Its Biomedical Applications. *Int. J. Nanomed.* **2023**, *18*, 4727–4750. [CrossRef] [PubMed]
36. Azad, A.; Zafar, H.; Raza, F.; Sulaiman, M. Factors Influencing the Green Synthesis of Metallic Nanoparticles Using Plant Extracts: A Comprehensive Review. *Pharm. Front.* **2023**, *05*, e117–e131. [CrossRef]
37. Khan, S.; Al-Qurainy, F.; Al-hashimi, A.; Nadeem, M.; Tarroum, M.; Shaikhaldein, H.O.; Salih, A.M. Effect of Green Synthesized ZnO-NPs on Growth, Antioxidant System Response and Bioactive Compound Accumulation in *Echinops macrochaetus*, a Potential Medicinal Plant, and Assessment of Genome Size (2C DNA Content). *Plants* **2023**, *12*, 1669. [CrossRef] [PubMed]
38. Miranda, A.; Akpobolokemi, T.; Chung, E.; Ren, G.; Raimi-Abraham, B.T. PH Alteration in Plant-Mediated Green Synthesis and Its Resultant Impact on Antimicrobial Properties of Silver Nanoparticles (AgNPs). *Antibiotics* **2022**, *11*, 1592. [CrossRef] [PubMed]
39. Velgosova, O.; Mačák, L.; Lisnichuk, M.; Varga, P. Influence of PH and Temperature on the Synthesis and Stability of Biologically Synthesized AgNPs. *Appl. Nano* **2025**, *6*, 22. [CrossRef]
40. Yaraki, M.T.; Zahed Nasab, S.; Zare, I.; Dahri, M.; Moein Sadeghi, M.; Koohi, M.; Tan, Y.N. Biomimetic Metallic Nanostructures for Biomedical Applications, Catalysis, and Beyond. *Ind. Eng. Chem. Res.* **2022**, *61*, 7547–7593. [CrossRef]
41. Blakey, I.; Merican, Z.; Thurecht, K.J. A Method for Controlling the Aggregation of Gold Nanoparticles: Tuning of Optical and Spectroscopic Properties. *Langmuir* **2013**, *29*, 8266–8274. [CrossRef]
42. İpek, P.; Baran, M.F.; Baran, A.; Hatipoğlu, A.; Keskin, C.; Yildiztekin, M.; Küçükaydin, S.; Becerekli, H.; Kurt, K.; Eftekhari, A.; et al. Green Synthesis and Evaluation of Antipathogenic, Antioxidant, and Anticholinesterase Activities of Gold Nanoparticles (Au NPs) from *Allium cepa* L. Peel Aqueous Extract. *Biomass Convers. Biorefinery* **2024**, *14*, 10661–10670. [CrossRef]
43. Banoo, S.; Pradhan, N. One-Step Synthesis of Stable Gold Nanoparticles Using *Aspergillus austwickii* CO1 and Its Application in Colorimetric Detection of Mg^{2+} Ion. *Chem. Pap.* **2024**, *78*, 6097–6113. [CrossRef]

44. Stalin, N.; Ramar, D.; Esakkirajan, M.; ArunPrasanna, V.; Arumugam, A.; Gopinath, K. Green Synthesis-Driven Gold Nanoparticles Using *Lilium wallichianum* Leaf Extract for Biomedical Applications. *Inorg. Chem. Commun.* **2025**, *178*, 114507. [CrossRef]
45. Specac Interpreting Infrared Spectra—Specac Ltd. Available online: https://specac.com/theory-articles/interpreting-infra-red-spectroscopy/ (accessed on 7 January 2026).
46. Shah, A.; Akhtar, S.; Mahmood, F.; Urooj, S.; Siddique, A.B.; Irfan, M.I.; Naeem-ul-Hassan, M.; Sher, M.; Alhoshani, A.; Rauf, A.; et al. *Fagonia arabica* Extract-Stabilized Gold Nanoparticles as a Highly Selective Colorimetric Nanoprobe for Cd^{2+} Detection and as a Potential Photocatalytic and Antibacterial Agent. *Surf. Interfaces* **2024**, *51*, 104556. [CrossRef]
47. Sukumaran, R.A.; Lakavath, K.; Phani Kumar, V.V.N.; Karingula, S.; Mahato, K.; Kotagiri, Y.G. Eco-Friendly Synthesis of a Porous Reduced Graphene Oxide–Polypyrrole–Gold Nanoparticle Hybrid Nanocomposite for Electrochemical Detection of Methotrexate Using a Strip Sensor. *Nanoscale* **2025**, *17*, 4472–4484. [CrossRef] [PubMed]
48. Supin, K.K.; Parvathy Namboothiri, P.M.; Vasundhara, M. Enhanced Photocatalytic Activity in ZnO Nanoparticles Developed Using Novel *Lepidagathis ananthapuramensis* Leaf Extract. *RSC Adv.* **2023**, *13*, 1497–1515. [CrossRef] [PubMed]
49. Ejaz, A.; Mamtaz, Z.; Yasmin, I.; Shaban, M.; Siddique, A.B.; Irfan, M.I.; Ali, A.; Muhammad, S.; Sameeh, M.Y.; Abbas, A. *Cyperus scariosus* Extract Based Greenly Synthesized Gold Nanoparticles as Colorimetric Nanoprobe for Ni^{2+} Detection and as Antibacterial and Photocatalytic Agent. *J. Mol. Liq.* **2024**, *393*, 123622. [CrossRef]
50. Kerdtoob, S.; Chanthasena, P.; Rosyidah, A.; Limphirat, W.; Penkhrue, W.; Ganta, P.; Srisakvarangkool, W.; Yasawong, M.; Nantapong, N. *Streptomyces monashensis* MSK03-Mediated Synthesis of Gold Nanoparticles: Characterization and Antibacterial Activity. *RSC Adv.* **2024**, *14*, 4778–4787. [CrossRef] [PubMed]
51. Kasi, G.; Thanakkasaranee, S.; Seesuriyachan, P.; Rachtanapun, P. One–Pot Synthesis of Gold Nanoparticles Using *Pandanus amaryllifolius* Leaf Extract and Their Antibacterial, Antioxidant, Anticancer, and Ecotoxicity Assessment. *Biocatal. Agric. Biotechnol.* **2023**, *50*, 102695. [CrossRef]

Disclaimer/Publisher's Note: The statements, opinions and data contained in all publications are solely those of the individual author(s) and contributor(s) and not of MDPI and/or the editor(s). MDPI and/or the editor(s) disclaim responsibility for any injury to people or property resulting from any ideas, methods, instructions or products referred to in the content.